Review Article

NMR IN BIOMEDICINE

Received: 7 December 2010, Revised: 25 August 2011, Accepted: 31 August 2011, Published online in Wiley Online Library: 21 November 2011

(wileyonlinelibrary.com) DOI: 10.1002/nbm.1794

7-T MR—from research to clinical applications?

Ewald Moser[a,b,c]*, Freddy Stahlberg[d], Mark E. Ladd[e,f] and Siegfried Trattnig[b,g]

Over 20 000 MR systems are currently installed worldwide and, although the majority operate at magnetic fields of 1.5 T and below (i.e. about 70%), experience with 3-T (in high-field clinical diagnostic imaging and research) and 7-T (research only) human MR scanners points to a future in functional and metabolic MR diagnostics. Complementary to previous studies, this review attempts to provide an overview of ultrahigh-field MR research with special emphasis on emerging clinical applications at 7 T. We provide a short summary of the technical development and the current status of installed MR systems. The advantages and challenges of ultrahigh-field MRI and MRS are discussed with special emphasis on radiofrequency inhomogeneity, relaxation times, signal-to-noise improvements, susceptibility effects, chemical shifts, specific absorption rate and other safety issues. In terms of applications, we focus on the topics most likely to gain significantly from 7-T MR, i.e. brain imaging and spectroscopy and musculoskeletal imaging, but also body imaging, which is particularly challenging. Examples are given to demonstrate the advantages of susceptibility-weighted imaging, time-of-flight MR angiography, high-resolution functional MRI, ^{1}H and ^{31}P MRSI in the human brain, sodium and functional imaging of cartilage and the first results (and artefacts) using an eight-channel body array, suggesting future areas of research that should be intensified in order to fully explore the potential of 7-T MR systems for use in clinical diagnosis. Copyright © 2011 John Wiley & Sons, Ltd.

Keywords: ultrahigh-field MR; 7 T; safety; brain; cartilage; skeletal muscle; heart; vascular

INTRODUCTION

About 40 years ago, the idea of using NMR as a basis for non-invasive imaging of the human body was formulated, in particular, by Paul C. Lauterbur and Sir Peter Mansfield. Since then, MRI has developed into one of the most flexible tools in medical research and diagnostic imaging, with well over 20 000 MRI systems worldwide in operation today and an annual turnover rate of about 3000 units.

The relatively short history of human MRI can hitherto be structured into four major periods related to field strength dependence.

1. During the early 1980s, MRI scanners using low (<0.5 T) or moderate (0.5 T < B_0 < 1.5 T) field strengths became instruments for morphological imaging and replaced or supplemented several conventional radiological methods. In the mid-1990s, sales started to decline and the mid-field range vanished completely, leaving low-field MR system sales at 15% by the end of 2009.
2. Following this development, the 1990s brought substantial technical improvements, making fast and ultrafast imaging sequences, such as echo planar imaging (EPI), possible. In parallel, it was shown that MRI techniques, primarily using a field strength of 1.5 T, had an enormous inherent potential for functional studies, e.g. metabolism, blood flow and associated tissue movements, molecular diffusion, capillary perfusion and cortical activation. In 2005, about 70% of all MR systems sold were operated at a field strength of 1.5 T, which then started to decline to about 65% by the end of 2009.
3. The most commonly selected step for commercial manufacturers when moving beyond 1.5 T towards the end of the

* *Correspondence to: E. Moser, MR Centre of Excellence, Lazarettgasse 14, A-1090, Vienna, Austria.*
E-mail: Ewald.moser@meduniwien.ac.at

a *E. Moser*
Centre for Medical Physics and Biomedical Engineering, Medical University of Vienna, Vienna, Austria

b *E. Moser, S. Trattnig*
MR Centre of Excellence, Medical University of Vienna, Vienna, Austria

c *E. Moser*
Department of Psychiatry, University of Pennsylvania Medical Center, Philadelphia, PA, USA

d *F. Stahlberg*
Department of Medical Radiation Physics, Department of Diagnostic Radiology and Lund University Bioimaging Centre (LBIC), Lund University, Lund, Sweden

e *M. E. Ladd*
Erwin L. Hahn Institute for Magnetic Resonance Imaging, University Duisburg-Essen, Essen, Germany

f *M. E. Ladd*
Department of Diagnostic and Interventional Radiology and Neuroradiology, University Duisburg-Essen, Essen, Germany

g *S. Trattnig*
Department of Radiology, Medical University of Vienna, Vienna, Austria

Abbreviations used: *BOLD, blood oxygen level dependent (contrast); Cho, choline-containing compounds; Cr, total creatine; CT, computed tomography; dGEMRIC, delayed gadolinium-enhanced MRI of cartilage; ECG, electrocardiogram; EPI, echo planar imaging; FCD, fixed charge density; FLAIR, fluid-attenuated inversion recovery; FLASH, fast low-angle shot; fMRI, functional MRI; GABA, γ−aminobutyric acid; GAG, glycosaminoglycan; Gln, glutamine; Glu, glutamate; Glx, sum of Gln + Glu; GRAPPA, GeneRalized Autocalibrating Partially Parallel Acquisition; ICNIRP, International Commission on Non-Ionizing Radiation Protection; mIns, myo-inositol; ISIS, Image Selected In vivo Spectroscopy; MPRAGE, magnetisation-prepared rapid gradient echo; NAA, N-acetyl-aspartate; PG, proteoglycan; RF, radiofrequency; SAR, specific absorption rate; SCA, spinocerebellar ataxia; SNR, signal-to-noise ratio; SWI, susceptibility-weighted imaging; Tau, taurine; TOF, time of flight; TSE, turbo spin echo; UHF, ultrahigh (magnetic) field.*

1990s was to double the field strength, i.e. to work at 3 T. The reasons for the selection of this field strength were many. The problems with radiofrequency (RF) inhomogeneities, as well as the increase in RF heating as measured by the specific absorption rate (SAR), were possible to handle, regulatory frameworks accepted this field strength for clinical use in the USA and Europe, and actively shielded magnets enabled the installation of 3-T units in hospital environments. As a consequence, high-field MRI at 3 T has now become the benchmark for clinical MRI research and qualified clinical investigations. Overall, the sales of 3-T systems presently lie at around 27% of the total market with a strong positive slope. The clinical benefits are many, e.g. combined morphological and functional high-field MR methods using this field strength have provided insights into new aspects of central nervous system function, and facilitated the early diagnosis of several brain pathologies (1). However, keeping the diagnostic quality of 1.5-T systems at half the scan time is an option for private radiological institutes, which need a high patient throughput because of economical pressure. Since the introduction of commercial MR systems for clinical diagnosis, a clear trend towards higher field strength can be noted.

4. The next vital step was taken in the early 2000s (2–5) by increasing the MRI field strength by another factor of approximately two and, currently, at least three major MR vendors provide commercial 7-T units for human and clinical research under adequate ethical permission. Approximately 10 years ago, the number of ultrahigh-field (UHF) MR installations in the world was less than five. During recent years, the number of installations finalised or under preparation has increased to about 40 (0.2% of the installed base). This rapid increase indicates the growing interest in UHF MRI in the bioimaging community, brought about by initial (6–9) and more recent (10–16) results regarding morphological detail as well as functional imaging capability. Furthermore, rapidly evolving magnet technology is presently enabling the installation of human MRI scanners at field strengths above 7 T, although at significantly higher costs in comparison with 7 T, and with considerably more health and safety precautions for patients and staff. Higher fields for human brain MRI, such as 9.4 T, are already established (e.g. University of Minnesota, USA, since 2004; Max Planck Institute, Tubingen, Germany, since 2007; University of Illinois at Chicago, IL, USA, since 2007; Forschungszentrum Julich, Germany, since 2009). At present, systems are also planned or under establishment for human imaging at 11.7 T (e.g. Neurospin CEA, Saclay, France; National Institutes of Health, Bethesda, MD, USA). In addition, it may be stated that the majority of scanners installed so far are sited in either Europe or the USA, in approximately equal amounts. In Asia, Japan (University of Niigata) and South Korea (Gachon University of Medicine and Science) stand out in terms of UHF MR research.

Of paramount importance for the future clinical use of UHF MRI is that vendors are presently developing actively shielded scanners at 7 T. This technical development puts less demand on the installation site in terms of space required for the equipment in comparison with earlier passively shielded magnets. A step towards the 'second generation' of 7-T scanners can be seen and, within approximately 1 year, the first three to five 7-T actively shielded systems can be expected to be in operation.

ADVANTAGES OF UHF STRENGTH

There are several reasons for increasing the field strength in MR. First, an overview of potential benefits is given, with the reservation that several of the effects can act in both ways, i.e. be a benefit but also a drawback, as described in the later part of this section. A brief overview is provided in Table 1.

Enhanced sensitivity

A basic feature is the intrinsic increase in spin polarisation with field strength, opening up possibilities to increase the signal-to-noise ratio (SNR) and resolution significantly (4,5). The spin magnetisation is expressed by the formula:

$$M_0 = \rho_0 \frac{\gamma^2 \hbar^2}{4kT} B_0$$

where ρ_0 is the proton spin density, γ is the gyromagnetic ratio, $\hbar$ is the Planck constant divided by 2π, k is the Boltzmann constant, T is the absolute temperature (in kelvin) and B_0 is the static

Table 1. Brief overview of the potential advantages and disadvantages when increasing the magnetic field strength from 3 to 7 T (note that the consequences—positive or negative—may depend on technical and anatomical details)

Characteristic	Trend	Positive	Negative
SNR	↑	Higher resolution, shorter scan time, X-nuclei	n.a.
SAR	↑	n.a.	Fewer slices, smaller flip angle, longer breathhold
Physiological side-effects	↑	n.a.	Dizziness, nausea, metallic taste
Relaxation times	T_1 ↑	TOF, ASL, cardiac tagging	Longer scan time
	T_2 ↓		Diffusion-weighted imaging, diffusion tensor imaging
	T_2^* ↓	SWI, BOLD	
RF homogeneity	↓	Parallel reception, parallel transmission	Position-dependent flip angle, poor inversion, unexpected contrast
Susceptibility effects	↑	BOLD, SWI, T_2^*	Geometric distortions, intravoxel dephasing
Chemical shift	↑	Fat saturation, spectral resolution	Fat/water (metabolite) misregistration

ASL, arterial spin labelling; BOLD, blood oxygen level dependent; n.a., not applicable; SAR, specific absorption rate; SNR, signal-to-noise ratio; SWI, susceptibility-weighted imaging; TOF, time of flight.

magnetic field strength of the polarising field. Although the polarisation available scales linearly with the field strength in this formula, one must be careful to take into account several other factors to derive how the measurable signal and the noise vary with field strength in order to finally achieve an indication of how SNR increases. These factors include the linear frequency dependence of the Faraday voltage inductance in the receive coil and the determination of whether the noise is dominated by the sample itself or by the system hardware. Because the SNR is also proportional to the linear dimension of the voxel size, the most obvious application of increased sensitivity is obtaining a higher spatial resolution. The increase, however, is not always as significant as first expected, especially for three-dimensional imaging, where voxel sizes are generally isotropic and the increase in sensitivity must be invested in improving the resolution in each of the three orthogonal spatial directions. Assuming a linear increase in SNR with B_0, the achievable reduction in voxel size for two-dimensional imaging, whilst maintaining a constant slice thickness, scales with the square root of B_0 (i.e. the voxel dimensions can be decreased in plane by 1.53 when switching from 3 to 7 T). In this case, it is implicitly assumed that the field of view is simultaneously decreased by 1.53 to maintain the total number of signal samples. Assuming three-dimensional imaging with isotropic voxels, the decrease in linear voxel dimension is proportional to the cube root of B_0, i.e. a factor of only 1.33.

Of specific clinical interest for neurological applications is that different layers of the cerebral cortex can be seen at 7 T (generally not possible at lower field strengths) because of the improved image SNR, contrast-to-noise ratio and spatial resolution. At 7 T, a spatial resolution of 100–200 μm can be obtained, and this improvement may be used, for example, for the detection of changes in cortical structure as a first sign of early dementia, as well as for the visualisation of small lesions, vascularisation and myelin pathology in early multiple sclerosis (11,12). Cartilage imaging in different joints will also benefit from the high SNR for the mapping of subtle early degenerative changes.

Susceptibility as a contrast parameter

Another advantage is improved sensitivity to susceptibility effects/reduced T_2* relaxation times when compared with lower field strengths. Excellent vascular mapping can be performed at 7 T using susceptibility-weighted imaging (SWI) (13,14), when compared with 1.5 or 3 T (17), and the concept of SWI gives rise to completely new contrast possibilities at 7 T (18). One important step to the final processed SWI magnitude data is the computation of the filtered phase images (19). Although these phase images reflect susceptibility information, they are not maps of the actual susceptibility distribution. Nevertheless, the phase information available in MRI practically carries all the information that is needed to reconstruct the local magnetic source or susceptibility difference between tissues (20). Consequently, the more advanced concept of quantitative susceptibility mapping has been introduced recently (21) to create maps that can be used not only to differentiate paramagnetic from diamagnetic substances (22), but also to quantify the amount of a given substance present that is causing the susceptibility difference, such as local iron differences between tissues. Clinically, SWI makes it possible to image microbleeds and veins more effectively, whereas quantitative susceptibility imaging may provide methods to quantify oxygen saturation (23) or local iron content (24).

The susceptibility effects are also used, for example, in dynamic susceptibility contrast brain perfusion measurements and in cortical activation studies using blood oxygen level-dependent (BOLD) contrast. As one example, for BOLD imaging, a more than two-fold increase in ΔR_2* between rest and activation has been observed when comparing motor task functional MRI (fMRI) at 3 and 7 T. The increased BOLD contrast seen when increasing the field strength can be used to increase the resolution, thereby also optimising the relative influence of physiological noise in the BOLD experiment (15,16). For example, for studies of behaviour, learning and brain development, fMRI at 7 T holds significant promise for front-line research in the future (25).

Spectroscopic resolution and non-proton MRI/MRS

Other major improvements have encompassed increased spectral resolution in proton (^{1}H) MRS, allowing, for example, the identification of glutamine (Gln)/glutamate (Glu) (26). Standard ^{1}H MRI already allows excellent clinical diagnosis for many pathologies, even at 1.5 and 3 T. Despite the sensitivity achieved, however, the specificity remains a persistent problem. Therefore, nuclei other than protons may allow a more specific diagnosis because of a much closer relation to the underlying physiopathology. For example, sodium is an essential element for human life (as well as animals and plants). Sodium ions move across cell membranes, in opposition to potassium ions, to allow the organism to build up electrostatic charge across cell membranes. This allows, for example, the transmission of nerve impulses through the body. Sodium (^{23}Na) MRI is able to map the free sodium distribution in human tissue, which may help to diagnose stroke (27) or early cartilage damage (28). Sodium supports the osmoregulatory system and is essential to maintain the body's total fluid level. Another MR-sensitive nucleus important in tissue metabolism is phosphorus (^{31}P). As a result of the low sensitivity when compared with protons or even sodium, high-resolution imaging is not an option, not even at 7 T. A well-established MR method to follow (early) pathological changes in human tissue is MRS. This allows more complex changes to be followed in relevant metabolites and amino acids *in vivo* and non-invasively, provided that sufficient metabolite concentrations are present. This enables the detection of deficiencies, even in healthy subjects, for example, to improve physical training programmes or rehabilitation, and in various patient groups. In general, energy metabolism may be followed by ^{31}P MRS (29). Why have these methods not been used more widely in clinical diagnostics so far? There are several reasons, and the most important is sensitivity. All MR-visible nuclei other than protons are inherently less sensitive, i.e. provide a lower signal. In addition, the natural abundance may be lower, resulting in relative sensitivities of other biologically relevant nuclei of only 9.3% (^{23}Na), 6.6% (^{31}P), 2.9% (^{17}O), 1.6% (^{13}C) and 1% (^{15}N), when compared with ^{1}H (29). Second, when studying various tissue metabolites directly [abundant metabolites vary between 1 and 10 mmol, compared with water (about 35 mol in tissue)], another decrease in the sensitivity of the experiment is to be expected. As a consequence, poor localisation (i.e. large voxel size of >1 cm^3) or excessive total measurement times (>1 h), or both, have to be accepted. Although the wavelength required to excite protons at 7 T is about 10–12 cm, X-nuclei require a much longer wavelength, relaxing constraints in coil design and SAR. Therefore, 7-T systems may be a crucial step to foster clinical applications of non-proton MRS (30). Other reasons for the limited use of

MRS in clinical diagnosis are the application of sophisticated spectroscopy protocols, including fine tuning of the whole MR system, individual voxel positioning, extra local shimming and water or fat suppression in ^{1}H MRS. Furthermore, reference experiments and dedicated fitting algorithms (e.g. LCModel, jMRUI, etc.) have to be used in a sensible way to obtain actual metabolite concentrations. Finally, the interpretation of metabolic changes is less obvious than increases or decreases in image intensity. Altogether, this renders MRS in a clinical environment a less robust method when compared with MRI. Nevertheless, a boost to these so far 'exotic' MR applications can be expected, at least in specialised clinical applications (31).

Relaxation time alterations

With increasing field strength, the proton relaxation times of the tissues change as a result of characteristic dipole–dipole interaction, and a significant increase in T_1 is observed when moving from 1.5 to 3 and 7 T (32). The T_1 effect can be used advantageously for arterial spin labelling (28) and, perhaps with more general impact, for MR angiography owing to improved background suppression (16). However, non-proton relaxation times modulated by other relaxation mechanisms may show a quite different behaviour. For sodium, as a result of quadrupolar relaxation, T_1 times should be about the same at 3 and 7 T. However, phosphorus T_1 decreases significantly from 3 to 7 T for larger, asymmetric molecules (33), enabling localised, single-shot, dynamic MRS of skeletal muscle (34,35), which may be used to study metabolism *in vivo*. Very probably, chemical shift anisotropy causes the T_1 of phosphocreatine, phosphomonoesters and phosphodiesters to decrease with B_0, but not for the symmetric inorganic phosphate molecule.

Parallel transmission and imaging

It has been shown (36–39) that parallel imaging can be utilised with higher speed reduction factors at higher field strengths (for an equivalent amount of noise introduced by the so-called *g* factor), significantly reducing the acquisition time. Parallel transmission MR enables significant improvements in excitation uniformity and coverage; however, substantial research work still needs to be performed with respect to patient safety calculations (B_1, SAR, etc.) to fully develop safe and robust parallel transmit technology. In this context, is should be mentioned that a completely different approach, not utilising a transceiver close to the object, has been proposed recently (40). Using this so-called travelling wave technique, RF transmission and signal detection are made at a distance from the object itself. Although the concept is not yet fully developed and a homogeneous excitation field is similarly challenging to achieve as with conventional local resonators, it does open up new possibilities for manipulating RF excitation.

CHALLENGES OF ULTRA-HIGH FIELD STRENGTH

Throughout the history of MRI, an increase in field strength has always been associated with various problems. On the manufacturer side, increased field strength increases the technical challenges and costs. For the user, the potential improvements in image quality may well be counteracted by negative effects, such as an increased severity of artefacts, higher motion sensitivity, increased sensitivity to physiological noise, increased RF heating, etc. (see also Table 1). In this context, the step from 3 to 7 T has not been trivial, and some of the most well-recognised problems and challenges are briefly addressed below.

RF inhomogeneity

With increasing field strength, the Larmor wavelength for protons is reduced and, at 7 T, approaches the dimensions of the human body and larger organs. This introduces significant and often unpredictable inhomogeneities in the MR images, earlier recognised as 'dielectric resonances', but presently considered to be a result of destructive B_1 interference (41). It can be expected that the step from 3 to 7 T will enhance problems more significantly than moving from 1.5 to 3 T and, as an example, a central brightening effect is often observed at 7 T when imaging the brain using volume coils. As a first step, at 3 T as well as 7 T, 'flattening' filters have been proposed to smooth out signal inhomogeneities. A second step, utilising several coil elements during RF transmission, is denoted 'B_1 shimming' or 'RF shimming'. With this method, the phases and/or amplitudes of the coil elements are manipulated to obtain homogeneous excitation. A more advanced technique based on a theoretical framework presented in the late 1980s is parallel RF transmission (where gradient trajectories in excitation *k* space are followed during RF transmission from multiple coil elements to create spatially varying excitation profiles). This technique may mature in the future to become useful, in particular for clinical research at ultra-high fields (42–44).

Relaxation time alterations

For morphological imaging, the above-mentioned proton T_1 increase will, in general, lead to increased examination times. Perhaps even more problematic are the observed effects of T_2 reduction with increasing field strength, giving rise to difficulties in techniques relying on long TEs, such as diffusion-weighted imaging and diffusion tensor imaging. Taking into account increased susceptibility effects/shortened T_2*, conventional single-shot EPI techniques for diffusion-weighted imaging do not appear to benefit from the step from 3 to 7 T. However, recent combinations of parallel imaging techniques and segmented readout schemes have shown an increase in image quality in diffusion-weighted imaging at 7 T, thereby also providing promise for future high-quality diffusion tensor imaging at ultra-high field strengths (45). ^{1}H MRS and, in particular, MRSI may also yield a reduction in SNR when using echo-based localisation schemes, as a result of long TEs when compared with T_2 or T_2*.

Susceptibility effects

As stated above, similar to when moving from 1.5 to 3 T, one must expect increased susceptibility artefacts/T_2* shortening when moving from 3 to 7 T, giving rise to, for example, increased intravoxel signal loss and geometric distortion and, subsequently, reduced image quality in regions with large magnetic field inhomogeneities. Susceptibility effects are conventionally reduced by B_0 shimming, and first-order as well as higher order shimming availability are mandatory prerequisites for 7-T scanners, as well as for clinical scanners operating at lower field strengths. In contrast with conventional static shimming, where shim parameters are defined during the pre-scan phase and maintained during the entire scan, the concept of dynamic shimming (46) has been proposed recently for UHF MRI (47). With this

method, shim parameters are updated slice by slice during the scan; however, higher order shim coils are normally not actively shielded, and hence dynamic updating using such coils may result in significant eddy current effects. Other approaches include thinner slices/smaller voxels, *z* shimming, etc. However, increased susceptibility effects are also one of the benefits of the increased field strength in specific regions, such as the brain.

Slice selection in ^{1}H MRSI

Challenges at 7 T include chemical shift displacement errors, B_0 and B_1 inhomogeneities and short T_2 relaxation times, leading to unreliable fat/water suppression, signal variation or reduced spectral resolution. Several groups have developed approaches to address some of these limitations. Some have focused on short acquisition delays (TE*) or echo times (TE) to minimise the signal loss of short T_2 components (48–50). Chemical shift displacement errors were reduced by the application of adiabatic refocusing pulses (26,51,52) or the omission of selective refocusing pulses (48,49,53). Variations in the transmit B_1 field (B_1^+) were also reduced using adiabatic pulses (26,51,52), by the omission of refocusing pulses (48–50) and by the use of multichannel transmit coils (49).

SAR effects

The issue of tissue heating in MRI, normally measured using the parameter SAR, comprises one of the most complex challenges for UHF MRI. As SAR scales with approximately the square of the magnetic field, heating issues become a problem at 3 T, and are further enhanced at 7 T. In addition, the RF magnetic as well as electric fields vary spatially at 7 T, and hence local SAR variations are likely to occur.

Therefore, careful coil design and optimisation of pulse sequences when moving from 3 to 7 T are mandatory from a SAR perspective, with consequences on, for example, slice coverage and choice of repetition time (30,54). Indeed, local SAR variations may be further enhanced by the use of parallel transmit techniques (55), and it can be assumed that there are still significant improvements to be made before such techniques can be introduced into clinical research at 7 T.

In this context, 7-T systems will probably not be prepared for imaging using body coils during the next few years, although RF shimming techniques may reduce SAR (56) and promising imaging results have been demonstrated (57). However, this does not mean that only the brain can be studied at 7 T, as local transmit–receive coils for most body parts are already available (e.g. single-loop ^{1}H, ^{23}Na and ^{31}P coils and ^{1}H phased-array coils for extremities) or under development. In addition, a consequence of the short wavelength is that local SAR can be much better manipulated at 7 T.

Other safety aspects

Below 8 T, the Food and Drug Administration does not deem MR diagnostic devices to be a significant risk for adults, children and infants aged over 1 month. However, the International Electrotechnical Commission states that, when the main static magnetic field is higher than 4 T, the MR system is operating at the second-level-controlled operating mode, requiring the approval of investigational human studies protocols according to local requirements (e.g. local ethics committees) and medical supervision for all patients. It can be foreseen that ethical application procedures (already performed by several research sites) will be reduced in complexity with the number of active sites. Studies on safety and patient discomfort at 7 T are sparse to date, and magnetic and electric field effects cannot be independently modelled. Early studies indicate no clinically significant changes in vital signs, but transient electrocardiogram (ECG) artefacts have been observed (58). Weak cognitive effects have been reported (59), and it has been observed that the number of subjective side-effects is increased at 7 T relative to 1.5 T, but that 7 T is well tolerated by the majority of subjects (60). However, potential problems with patients and personnel moving within the much stronger B_0 gradient of an actively shielded magnet bore at 7 T must be handled properly.

With regard to occupational safety, regulations and recommendations vary across the world. Although occupational exposure to a static magnetic field is allowed up to 4 T in the International Electrotechnical Commission standard, nation-specific static field occupational standards vary substantially. As an example, the National Radiological Protection Board in the UK states a whole-body maximum exposure of 2 T, whereas the Australian Radiation Laboratory recommends a limit of 5 T. In addition, such standards are frequently combined with a 'dose' limit, reducing the acceptable time spent per day in the environment (61).

In this context, it must be emphasised that, in 2004, the EU Physical Agents 2004/40/EC Directive on the minimum health and safety requirements regarding the exposure of workers to the risks arising from electromagnetic fields was approved. This Directive governs exposure to time-varying electromagnetic fields regardless of application, and is, to a large extent, based on guidelines published in 1998 by the International Commission on Non-Ionizing Radiation Protection (ICNIRP). Several international organisations, including the International Society for Magnetic Resonance in Medicine, European Society for Magnetic Resonance in Medicine and Biology and the European Coordination Committee of the Radiological, Electromedical and Healthcare IT Industry, at an early preparatory stage, warned about the consequences of the Directive in the field of medical MRI, as it was very likely that the Directive could influence MRI practice at conventional as well as at UHF strengths. As a consequence of the debate, the Directive was postponed until 2012. In 2009, ICNIRP published new guidelines concerning static magnetic fields (62), where it is stated that, "It is recommended that occupational exposure of the head and trunk should not exceed a spatial peak magnetic flux density of 2 T. However, for specific work applications, exposure up to 8 T can be permitted, if the environment is controlled and appropriate work practices are implemented to control movement-induced effects." Recently, ICNIRP also published its new guidelines concerning time-varying electric and magnetic fields (1 Hz to 100 kHz) (63) and, at present, the community awaits a rewritten EU Directive proposal.

Despite foreseen changes in the presently postponed EU Directive, it is mandatory that, when establishing a 7-T site in an EU country, the ongoing debate regarding the Directive and its future implementation in the member states is carefully monitored.

Costs of installation, system hardware and running a 7-T MR system

Currently, i.e. mid-2011, the installation of a second-generation, actively shielded, 7-T whole-body system requires an equipment

investment on the order of 7 M€, or approximately 1 M€/T, not including costs for service contract, building construction, staff and future hardware upgrades. As a consequence, in some European countries (e.g. Sweden and Denmark), the first 7-T scanner installed will be considered as national infrastructure. In this context, it should be noted that the costs mentioned as a general rule do not include a comprehensive set of coils for the whole human body, in part because several coils that are 'standard' at lower field strength have not yet become commercial products, either from MR system manufacturers or third party vendors. At this time, potential 7-T users should be aware of this, and of the necessity for future investments in RF coils. As an alternative, several active 7-T sites build their own coils, and hence a large group of physicists and engineers is required to run a 7-T installation. As a result of the commonality of the graphical user interface with clinical MR systems, however, radiographers are now starting to operate 7-T systems in clinical research (64).

In summary, although it will probably take some years before whole-body investigations can be performed routinely with high quality, the potential for basic morphological research, advanced functional research and molecular imaging is vast at 7 T, and significant progress in knowledge can be expected to result from the use of anatomical, functional and spectroscopic MRI at 7 T for studies of, for example, degenerative brain diseases. Hence, this next step in UHF MR has the potential to open up completely new pathways in morphological and functional imaging, and may also enable MRI to have a significant impact in the field of molecular and metabolic imaging, using MRS as well as in combination with positron emission tomography. In the sections below, different areas of application, taking advantage of the changes summarised above, are reviewed in more detail.

BRAIN IMAGING AT 7 T

Tumours and metastases

The significantly enhanced sensitivity at 7 T may prove to be a decisive advantage for the diagnosis of tumorous entities (65). The increased sensitivity to susceptibility artefacts can be used, for example, to make haemosiderin visible in an SWI sequence; such haemosiderin deposits may be associated with bleeding within tumours or metastases. The appearance of venous vessels is also markedly increased by the enhanced artefact extent (Fig. 1). This may be helpful in revealing the vascular distribution and possible neovascularisation in primary brain tumours (66). Gliomas can be well depicted with conventional field strengths. A marked improvement in spatial resolution in the T_2- or T_1-weighted sequences, although visually appealing, will have little influence on therapy and thus will be of minor clinical relevance. The improved representation of vessel-rich areas, however, could be of relevance. These areas should be indicative of higher malignancy. A more accurate target determination might therefore be conducted before a stereotactic biopsy. In addition to other techniques, such as MRS, the visualisation of augmented vascular presence could be a further component in the assessment of primary brain tumour malignancy. However, a higher applied field strength is not always clearly advantageous. In one small preliminary study, the detection of metastases of bronchial carcinomas in contrast-enhanced magnetisation-prepared rapid gradient echo (MPRAGE) was almost equivalent to the sensitivity at 1.5 T (67). It can be concluded that a more sensitive staging for patients with certain primaries may be possible at 7 T, but SWI will most likely provide the decisive difference rather than the T_1 sequence after the administration of the gadolinium contrast agent.

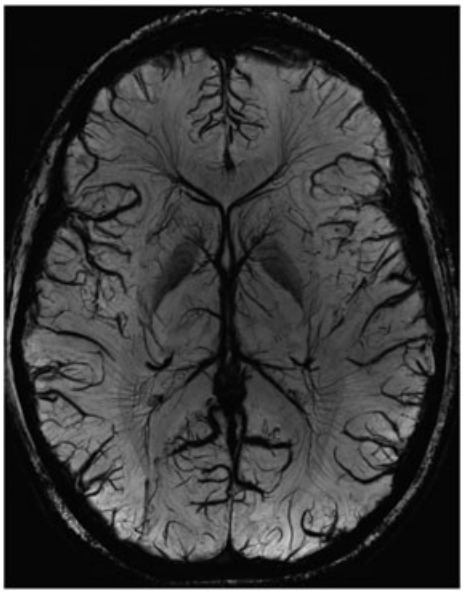

Figure 1. Susceptibility-weighted image revealing enhanced sensitivity to cerebral veins at 7 T.

Hippocampus

The hippocampus is a challenging structure to depict at low fields because of its small size and rich structure, and, at 7 T, because of its proximity to the skull base. The high-resolution depiction of the hippocampi is possible at 7 T without significant artefacts with proton density, T_2 and T_2* sequences, but also with T_1 MPRAGE, with an isotropic resolution of 0.5 mm (68). Even subfields of the internal hippocampal anatomy can be visualised with excellent resolution (68,69), which motivates the search for clinical applications. Cryptogenic epilepsy, for instance, remains an unresolved problem; in these patients, no structural abnormality can be diagnosed at MRI up to 3 T (70). The higher resolution of 7-T MRI would appear to be beneficial, and is currently being evaluated; initial investigations have been conducted in patients with known mesial sclerosis (71). Still missing is the examination of patients with a known temporal focus in the electroencephalogram, but occult lower field imaging results. In such cases, a detectable structural change would clearly have therapeutic relevance. Also of interest are the hippocampal changes associated with dementia of Alzheimer type. High-resolution SWI at 7 T has, for example, already successfully demonstrated the direct visualisation of pathology in the parietal association cortex in patients with Alzheimer's disease (13), and hippocampal volumetry appears to be facilitated at 7 T (72). Finally, a preliminary study has identified the prolongation of T_2* relaxation times in certain hippocampal subfields of patients with major depressive disorder (73).

Microangiopathic changes

In the radiological work-up of patients with dementia, vascular dementia plays a major role. A requirement is the detection of cerebral microangiopathy, which can be established in both computed tomography (CT) and clinical MRI (74). In the

pathogenesis of these white matter changes, arterial hypertension is considered to be the main cause, so that such changes are found not only in patients with dementia, but in many patients with cardiovascular disease. Hypertension is, in principle, amenable to treatment; the compliance of these patients is, however, often low. Visualisation of the changes in an individual's brain, which are well represented in a fluid-attenuated inversion recovery (FLAIR) sequence, could perhaps improve compliance by demonstrating them to the patient.

UHF is certainly not necessary for this, although FLAIR contrast is obtainable at 7 T (75,76). In the case of such microangiopathic white matter changes, a T_2*-weighted or SWI gradient echo sequence should certainly be added to the clinical work-up. These sequences are particularly sensitive to susceptibility artefacts as may originate from haemosiderin deposits in brain tissue. This allows the identification of small microbleeds that can occur in patients with microangiopathy, even if the microangiopathic changes themselves are not yet very pronounced. Previous investigations have shown a correlation between the number of microbleeds and the extent of cognitive deficits (77). Furthermore, it has been proposed that, in patients with microbleeds, secondary prevention measures with anticoagulants should be reconsidered (78,79). Currently, there is evidence that microbleeds are an important criterion with regard to microangiopathies and can be evaluated with clinical MRI today. With the help of higher field strengths, such as 7 T, the detection limit for microbleeding can be improved significantly (80). If many microbleeds have been established at 1.5 or 3 T, the patient does not need to undergo a 7-T MRI, but if anticoagulant therapy is planned in a patient with known microangiopathy and often co-existing cardiovascular pathologies, one should be as certain as possible that no microbleeding exists, so that the prophylactic therapy can be individually adapted and large intracerebral bleeds prevented. In such cases, the more sensitive detection method, including SWI, might be important and helpful.

Multiple sclerosis

For multiple sclerosis, MRI has long been a crucial imaging modality, and MRI is of major importance for the clinical assessment of patients with this disease. Essential sequences include a proton density and T_2-weighted turbo spin echo (TSE), FLAIR and a sagittal T_2-weighted TSE through the corpus callosum. Also important is a T_1-weighted sequence after contrast administration. Furthermore, a diffusion-weighted sequence is frequently performed to potentially detect active foci.

However, a definitive statement about the progression and severity of the disease is not generally possible, even when using multiple radiological parameters. In the context of the first appearance of clinical symptoms, MRI can often diagnostically confirm multiple sclerosis. Some lesions, however, cannot be depicted or are only very poorly depicted at 1.5 or 3 T. This is important if, for example, this is the only lesion in the patient. In particular, cortical lesions are often difficult to depict; imaging at 7 T, with increased resolution, can be more successful in this regard (11,81–83). Moreover, it is possible to reveal the anatomical features of the plaques almost microscopically. The typical localisation of the plaques around small venules can, for example, be clearly shown (84,85). This ability might provide an additional radiological differentiator between multiple sclerosis lesions and microangiopathic white matter lesions (86). It has also been observed that a subset of lesions is surrounded by a dark ring in T_2*-weighted images (11,87). These rings are also clearly visible on phase images. The rings are consistent with histological data indicating iron-containing macrophages in the lesion periphery (89). Here, quantitative SWI could be added to the protocol (22).

Angiography

With increasing field strength, proton T_1 relaxation times are prolonged, which is anticipated to benefit time-of-flight (TOF) angiography. Combined with the much higher spatial resolution, which can be implemented as a result of enhanced sensitivity, the depiction of much finer vessel branches is achievable (88–90). With this technique, it is possible to depict very small blood vessels, such as the lenticulostriate arteries (91,92). Even perforating arteries with their origin in the posterior communicating artery can be visualised at 7 T (93).

Thus far, it has been shown that a reliable depiction of all diagnostically relevant intracranial vessels is possible. Various gradient echo sequences can be used [TOF, interpolated three-dimensional fast low-angle shot (FLASH) and MPRAGE] (94,95). As a result of the increased resolution (better than $0.5 \times 0.5 \times 0.5\ mm^3$), the intracranial vessels can be traced far into the periphery (Fig. 2). The use of MPRAGE to depict the intracranial vessels only becomes feasible at UHF strength, because, at lower field strengths, the vasculature contrast is not sufficient. This option opens up new possibilities in the diagnosis of intracranial vascular changes. In addition to the vessels themselves, which appear hyperintense without contrast medium as in TOF MR angiography, the perivascular structures are well depicted and can be assessed in the source images. Further evaluations are needed to show, for example, how this precise registration (96,97) between vessels and parenchyma can be helpful in the work-up of vascular stenosis. It is possible that this approach can make the additional acquisition of a CT scan to visualise wall calcifications superfluous. It is important to depict such calcifications when considering endovascular therapy.

Figure 2. Maximum intensity projection of high-resolution whole-brain time-of-flight (TOF) MRI of a healthy volunteer acquired with a 32-channel head coil (Nova Medical, Wilmington, MA, USA) at 7 T.

Figure 3. Volume rendering of time-of-flight (TOF) MR angiography at 7 T in a patient with a basilar tip aneurysm (arrow). The absence of the left posterior communicating artery is well visualised.

Another possible clinical application is the depiction of aneurysms. It is known that small aneurysms may pose a bleeding risk, so that even these small structures should be reliably detectable with a non-invasive method. So far, however, TOF MR angiography at lower field strength is limited, in that aneurysms smaller than 3 mm may not always be detected. The higher resolution and improved contrast at 7 T might be very helpful. It must be remembered, however, that TOF MR angiography at high field strength is subject to increased artefacts. Initial results have shown advantages of UHF, but further investigations are needed to evaluate the clinical relevance of these benefits (98,99) (Fig. 3).

Cerebral cavernous malformations

The detection of intra-axial cavernomas by MRI is based on the appearance of susceptibility artefacts in gradient echo sequences. The precise anatomy, particularly of small lesions, often remains obscured at field strengths up to 3 T. The more centrally such a lesion is located, the more imperative it is to estimate the risk of bleeding *versus* the risk of surgical removal. In a recent study, it was verified that intracranial cavernous haemangiomas, which had already been detected at 1.5 T, could be depicted at 7 T after the optimisation of T_2*-weighted gradient echo sequences (100). A significant increase in spatial resolution could be achieved with SWI sequences. Such sequences result in a more sensitive detection of haemosiderin deposits at 1.5 and 3 T, and hence of cavernous haemangiomas; at 7 T, however, the influence of susceptibility is enhanced significantly. Thus, two factors, spatial resolution and susceptibility sensitivity, come together to significantly improve the depiction of cavernomas and, in particular, to enhance the sensitivity for detection. In the assessment of clinical relevance, it will be important to determine whether additional cavernomas can be found in eloquent regions, and to reliably assess whether there is an associated cavernous haemangioma in the presence of a developmental venous anomaly (101).

Cerebellum and cerebellar nuclei

More and more is becoming known about the pathogenesis of many hereditary ataxias, including Friedreich's ataxia and the most common autosomal-dominant spinocerebellar ataxias: SCA1, SCA2, SCA3 and SCA6. Because of the slowly progressive nature of these degenerative diseases, the establishment of biomarkers is of particular interest.

In the search for suitable MRI parameters for disease progression, UHF MRI provides a number of potential advantages compared with conventional field strengths. With conventional and voxel-based morphometry, the degree of atrophy of the cerebellum and its subsections can be detected, and the degree of cerebellar atrophy has been found to correlate with clinical ataxia scores (102,103). An open question remains how long the minimum appropriate time intervals must be in order to capture, for example, the natural disease progression using MR volumetry. It is likely that the sensitivity increases with higher spatial resolution. UHF MRI offers the capability of submillimetre resolution. However, the use of semi-automatic evaluation routines is complicated by the increased inhomogeneity in grey matter.

Furthermore, UHF MRI offers the opportunity to more accurately depict the fine structure of the cerebellum. Hereditary ataxias affect the cerebellar cortex and nuclei to varying degrees. In Friedreich's ataxia and SCA3, degeneration of the cerebellar nuclei is dominant, particularly of the dentate nucleus. In the case of SCA1, SCA2 and SCA6, however, the cerebellar cortex is particularly affected. The dentate nucleus and other cerebellar nuclei can be depicted at very high resolution using 7-T MRI (104). In addition to determining the nuclear volume, the assessment of possible changes in the iron content of the dentate nucleus is of interest. For an increasing number of neurodegenerative diseases, it has been proposed that an altered iron metabolism plays a role in pathogenesis (105). In Friedreich's ataxia, frataxin deficiency leads to impairment of cellular iron metabolism, and the dentate nucleus is particularly vulnerable because of its high iron content. The iron content in the brain can be examined by MRI based on the effect that iron leads to a shortening of the T_2 and T_2* relaxation times (106). As this effect increases with increasing field strength, it is likely that 7 T will bring further advantages, as has been shown for 3 T compared with 1.5 T.

Unlike in Friedreich's ataxia and SCA3, the cerebellar cortex is particularly affected in SCA1, SCA2 and SCA6. In animal studies using UHF MRI, the molecular layer could be rendered distinct from the granular layer (107). In the aforementioned forms of SCA, changes in the granular layer and the molecular layer have been described, in addition to degeneration of the Purkinje cells (108). UHF MRI examinations with corresponding spatial resolution would be one potential way to better understand the pathophysiology of the disease over its course.

Clinical fMRI

With the increasing field strength of available magnets, fMRI continues to gain importance in cognitive neuroimaging. The BOLD signal increases appreciably with increasing field strength, as it benefits doubly from both the higher SNR and the increased susceptibility sensitivity. This makes it possible, among other prospects, to use fMRI to examine individual events without the need for repetitions of the active stimuli in contrast with the rest condition, enabling new paradigms. Furthermore, a significantly improved spatial resolution is possible, so that activations can be represented at millimetre resolution (7,109). As a result of the increased BOLD sensitivity, standard smoothing (Fig. 4, top) is no longer required, enabling single-patient activation maps and more specific functional diagnostics (Fig. 4, bottom).

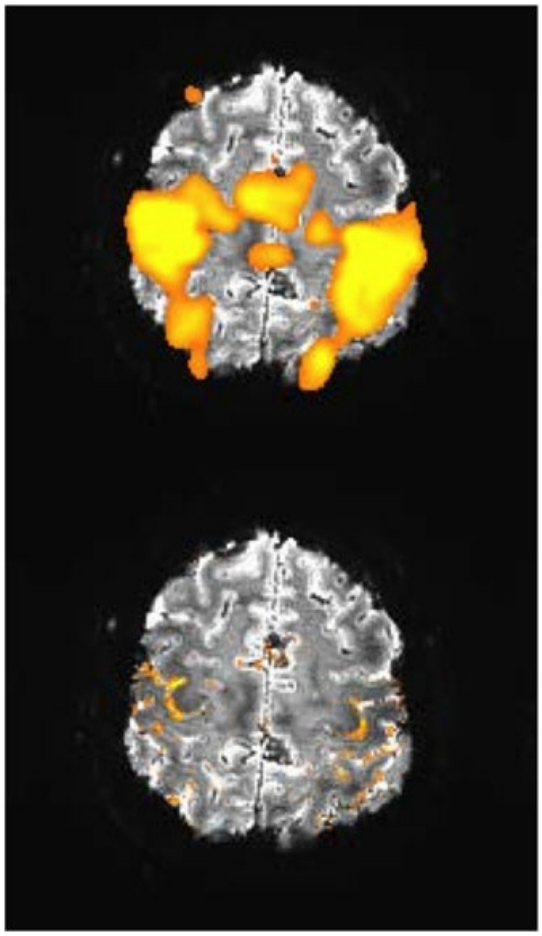

Figure 4. Single-subject, high-resolution (1 mm^3 isotropic) functional MRI map of the human motor cortex at 7 T using a 24-channel head coil (TE/TR = 34/2000 ms; GRAPPA = 4). Top: standard 6-mm Gaussian kernel smoothing of individual activation map. Note the strong blurring into white matter as a result of smoothing. Bottom: note that brain activation is significant only in grey matter (and, partly, in cerebrospinal fluid as a result of contamination), but not in white matter (familywise error corrected, $p < 0.05$, unsmoothed). Courtesy of C. Windischberger, Vienna, Austria [for more details, see ref. (110)].

However, fMRI at ultra-high field strengths is not straightforward: part of the benefits, which enable an increased BOLD contrast, can also lead to major problems. The increased sensitivity to susceptibility artefacts often leads to significant disturbances in BOLD imaging; in particular, echo planar sequences (EPI) are very vulnerable to these artefacts, so that the sequences must be suitably optimised for fMRI at 7 T (110).

Cerebrum

As at lower field strengths, the question arises: What is the possible clinical benefit of fMRI at 7 T? The most common clinical application of fMRI is the representation of eloquent areas before tumour removal. Typically, this involves motor or linguistic paradigms, which can be applied at 7 T similar to at lower field strengths. However, tumours are often located near the brain surface or close to the skull sinuses. This may lead to problems with susceptibility artefacts, although certain vital brain areas (e.g. motor, visual, temporal) might still be located in magnetically homogeneous parts of the brain. An optimisation of the measurement sequences and suppression of artefacts can be achieved by the application of multichannel coils. With these coils, it is possible to apply parallel imaging, which especially benefits from ultra-high fields (39). With parallel imaging, distortions are reduced significantly, although at the cost of decreased SNR, which in turn is important to enable precise overlay on high-resolution structural images in patients. The success of fMRI can be significantly greater at 7 T, particularly in cancer patients, as the increased signal facilitates good activations even with limited subject compliance. A very recent study in 17 patients with tumours performed presurgical localisation of the primary motor hand area, a rather benign area in terms of magnetic field homogeneity, comparing 3-T and 7-T results based on identical investigational procedures and comparable system-specific sequence optimisations. Significantly higher functional sensitivity was obtained at 7 T, as shown via the percentage signal change, mean *t* values, number of suprathreshold voxels and contrast-to-noise ratio. However, the 7-T data suffered from significantly increased ghosting and head motion artefacts (111). To what extent this advantage is relevant to clinical practice, i.e. treatment options and survival rate, and whether this gain is achievable in more difficult brain areas, will need to be examined in future studies.

Cerebellum

A large number of studies at conventional field strengths show activations of the cerebellar cortex, the main input structure of the cerebellum, and these studies have contributed significantly to a better understanding of the physiology of the cerebellum. For example, for some time, the cerebellum has been assigned not only motor but also non-motor functions (112,113). However, there are currently very few studies that have been able to demonstrate activation of the cerebellar nuclei, the main output structure of the cerebellum (114,115). The increased sensitivity and improved spatial resolution of UHF MRI could change this in the future. There are several reasons why the cerebellar nuclei may be activated less reliably than the cerebellar cortex. First, the iron content of the nuclei is high, which, on the one hand, facilitates the structural depiction of the nuclei via susceptibility artefacts, but, on the other, reduces the available BOLD contrast through signal voids (116). Another reason is the small size and geometry of the nuclei, which leads to dominance of partial volume effects. Even with voxel sizes of a few cubic millimetres, almost all voxels contain both white matter and nuclear constituents, and the former contribute little or nothing to the activation (117). Indeed, a good portion of the improved sensitivity of UHF MRI probably derives from the reduced voxel size and, consequently, the reduced partial volume effects (118). A third reason may be the cellular physiology of the BOLD effect, resulting in lower signal changes in the cerebellar nuclei than in the cortex.

The improved SNR of UHF MRI increases the probability of detecting activation of the cerebellar nuclei. However, confounding problems, many of which are particularly marked in the posterior cranial fossa, counteract part of the improved SNR. EPI BOLD near air–tissue interfaces, such as the sinuses or the ear canals, and the pulsation of cerebrospinal fluid and large blood vessels lead to signal dropouts, distortions and other artefacts. Head coils, imaging techniques and pulse sequences need to be further optimised for application at UHF. ECG, pulse and respiratory triggering are possibilities to minimise the effects of physiological motion in the posterior fossa.

Technical problems remain to be resolved, including motion artefacts, but UHF MRI promises reliable activation of the cerebellar nuclei, in addition to an improved spatial resolution of the cerebellar cortex. For example, reliable single-subject activation of the ventral brain, i.e. bilateral amygdala, bilateral fusiform gyrus/fusiform face area, orbitofrontal cortex, bilateral ventrolateral prefrontal cortex, can be obtained for a task comparing emotional faces *versus* objects of similar size, shape and luminosity (Fig. 5, top). Despite the solid activation map obtained after smoothing (top and bottom left), parameters estimated reflecting the specificity of brain activation are much greater when taken from the unsmoothed activation map (bottom right). Initial 7-T fMRI studies also show that activation of the dentate nucleus can, for example, be reliably achieved by finger movements (119). As it is likely that the quality of fMRI of the brainstem will improve in parallel in a similar way, activations of the red nucleus and the inferior olivary nucleus should be more readily detectable (120). The investigation of cerebellar control circuits in humans would then become feasible.

So far, the neuroimaging community has focused its research mainly on 3-T units as they are more widely available, easy to operate—even without a team of experts from physics and radiology—and much cheaper, including a 32-channel head coil. In addition, standard fMRI processing software is fine tuned for 1.5- and 3-T data. However, this approach may not ensure the scientific rigour and state-of-the-art data acquisition and processing required (121). Multidisciplinary research projects employing high-resolution fMRI protocols (see, for example, Figs 4 and 5) should stimulate the use of 7-T scanners and, in this way, help to better explore the potential of UHF fMRI in the neurosciences.

Brain metabolism

Although ^{1}H MRS at 1.5 T was approved by the Food and Drug Administration several years ago, it is still not in wide clinical use; 3-T and 4-T systems have helped to improve the sensitivity and specificity in ^{1}H MRS (122–124). The three major metabolites, i.e. *N*-acetyl-aspartate (NAA), total creatine (Cr) and choline compounds (Cho), are reliably accessible, whereas other important metabolites, such as myo-inositol (mIns), strongly overlap with other metabolites, and the amino acids Gln and Glu are not well separated and thus summed to yield Glx, limiting specificity (125). Furthermore, $\gamma-$aminobutyric acid (GABA) and glucose detection and, most importantly, quantification are rather limited (125). Here, 7-T MR may provide the requisite extra degree of sensitivity and spectral dispersion to increase specificity in both directions, anatomically (smaller voxel size) and spectrally (distance between peaks on the frequency axis) (126,127).

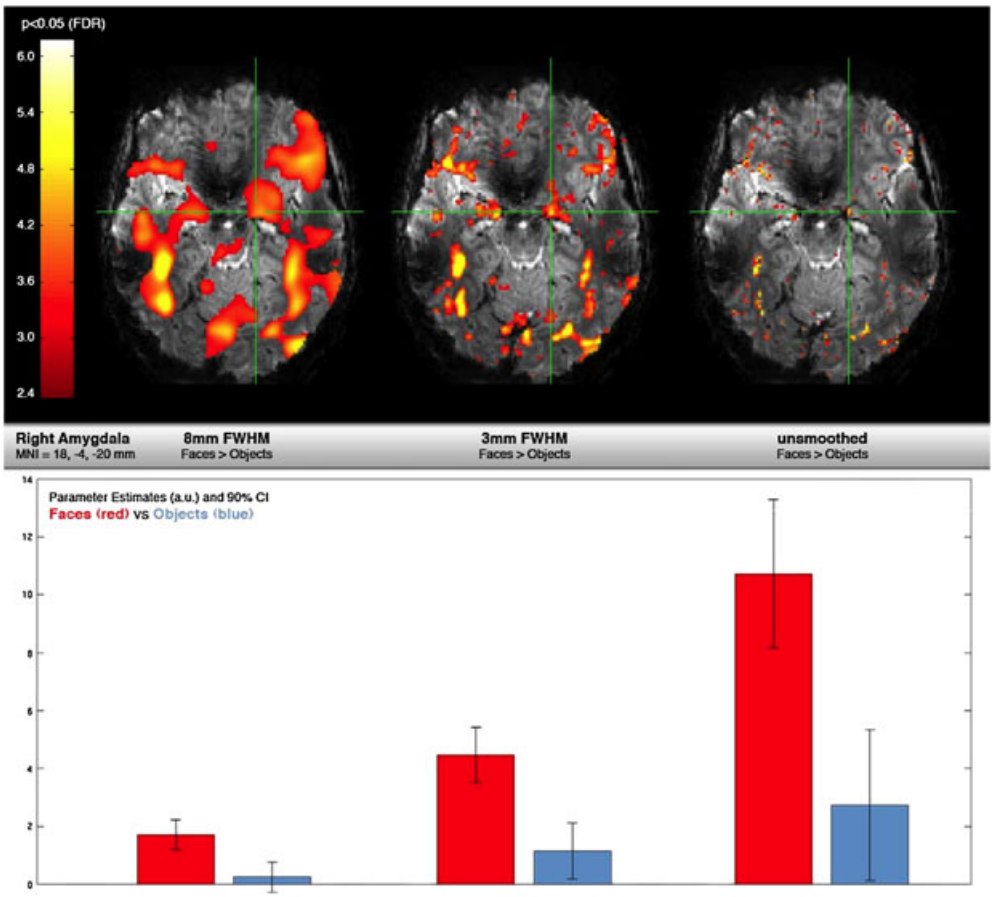

Figure 5. Single-subject functional MRI of the whole brain at 7 T using a 32-channel head coil (TE/TR = 23/1400 ms; GRAPPA = 4; 30 slices; 1.5 × 1.5 × 2 mm^3): difference map after viewing emotional faces *versus* objects. Brain activation is significant particularly in the ventral brain, i.e. bilateral amygdala, bilateral fusiform gyrus/fusiform face area, orbitofrontal cortex and bilateral ventrolateral prefrontal cortex. Top left: standard 8-mm Gaussian kernel smoothing; centre: reduced smoothing (3 mm); right: no smoothing. Bottom row displays the corresponding β values for the hypothesised right amygdala activation (red, emotional faces; blue, objects). Note the increasing specificity with increasing spatial resolution. FWHM, full width at half-maximum. Courtesy of C. Windischberger, Vienna, Austria.

Single-voxel spectra of high quality may be obtained from small volumes (Fig. 6), although peak assignment is not always straightforward [e.g. the lactate peak—about 0.5 mM *in vivo*—might be affected by residual, unsuppressed water side-bands or lipids from outside the volume of interest (128), and the taurine (Tau) peak might be 'contaminated' by glucose]. This may be used to characterise and follow up larger single lesions in multiple sclerosis or epileptic foci in the hippocampus.

Furthermore, pathological alterations are more often distributed across larger parts of the brain, and therefore spectroscopic imaging might be more valuable in clinical diagnosis (129). Although UHF ^{1}H MRSI is one of the most promising methods for the assessment of brain tissue and pathological changes, there are several challenges to be met, as listed in the Introduction. Adding to common knowledge, it has been demonstrated that higher order shimming of the brain at 7 T results in massive improvements in B_0 homogeneity, aiding, in particular, functional (EPI) and spectroscopic (MRSI) measurements when compared with typical first- and second-order shims implemented in clinical systems (130). Some groups have improved the suppression of subcutaneous lipid signals, whereas others have aimed to optimise the detection of specific amino acids. For example, Glu (9,131) and/or Gln (132), important in epilepsy, as well as Tau and GABA, can be detected directly via ^{1}H MRS at 7 T, and even glycine becomes visible (134). In some cases, however, improvements in spectral quality have led to increasing SAR (26,48).

Recently, Henning *et al*. (48) have presented a method based on free induction decay acquisition, with optimised outer volume suppression, which offers reduced sensitivity to B_1^+ errors, small chemical shift displacement errors and short TE*. Although quantification was complicated because of phase problems, robust quantification was achieved when first-order phase errors were taken into account for the quantification. Boer *et al*. (130) and Bogner *et al*. (134) further improved this approach to enable high-resolution (64 × 64) metabolic (NAA, *N*-acetyl-aspartylglutamate, Cr, Cho, mIns) and amino acid (Glu, Gln, Tau) mapping of the human brain in a reasonable measurement time. High spatial resolution results have been obtained, resulting in excellent separation of grey and white matter voxels in the brain, achieved with high sensitivity because of ultrashort TE* (1.3 ms). Thus, no or negligible loss as a result of chemical shift displacement, T_2 or *J* modulation was observed (Fig. 7). To keep the overall measurement time reasonable (30 min), TR had to be kept short (0.6 s) and T_1 correction was required. Nevertheless, lipid suppression was robust and SAR was still low (about 20% of the regulatory limits) and did not pose a limiting factor. The high spatial resolution significantly reduces contamination (blurring) between voxels located in different tissue types, reduces the linewidth and therefore allows for full separation of Glu and Gln, similar to the 10 times larger single-voxel spectrum (Fig. 6).

Nevertheless, the absolute quantification of metabolites and amino acids remains challenging because of variable baseline contributions from macromolecules. In this respect, Pan *et al*. (132) demonstrated that a macromolecule baseline may be acquired for correction using *J*-refocused coherence transfer MRSI, also showing data from an epilepsy patient. As concluded by Hetherington (135), 'the concept of a network of injury has emerged in the treatment of epilepsy.' The use of not only ^{1}H but also ^{31}P MRSI at 7 T (30) is supported by very recent data from Bogner *et al*. (136). Figure 8 shows a ^{31}P spectrum from the healthy human brain acquired in only 3 min. Clearly, the data quality in terms of sensitivity and spectral resolution would be sufficient for clinical studies. Spatial resolution could be increased using phased array receive coils for phosphorus, although at longer acquisition times. Gaining fully from the increased SNR and decreasing T_1 values relative to those obtained at 3 T (33,137), brain injury associated with a variety

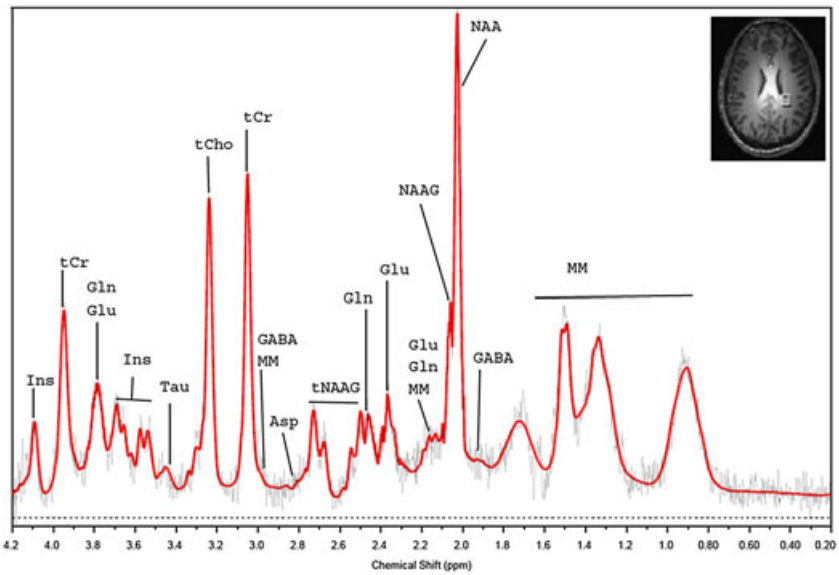

Figure 6. A 1.7-mL single-voxel ^{1}H spectrum at 7 T (TE/TM/TR = 20/25/3000 ms) from a parietal white matter region next to the left ventricle (see inset). The grey line represents original data and the red fitted line was obtained via LCModel [SNR(NAA) = 19, LW = 8 Hz]. Based on the high sensitivity and specificity (spectral dispersion), several metabolites can be reliably identified, including glutamine (Gln), glutamate (Glu) and glucose/taurine (Tau). Lactate, however, is contaminated by lipids. Asp, aspartate; GABA, γ-aminobutyric acid; Ins, inositol; LW, linewidth; MM, macromolecules; NAA, *N*-acetyl-aspartate; NAAG, *N*-acetyl-aspartylglutamate; SNR, signal-to-noise ratio; tCho, total choline; tCr, total creatine; tNAAG, total NAAG. Courtesy of O. Speck, Magdeburg, Germany [to be published in J. Neurol. Neurochir. Psychiatr. (2011)].

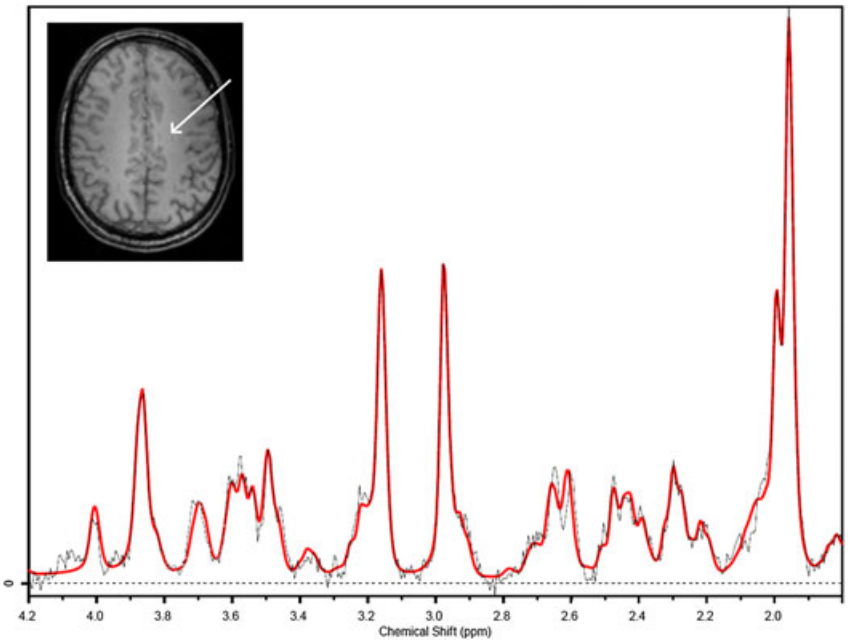

Figure 7. High-resolution 7-T ^{1}H spectrum after zeroth-order and first-order phase correction (voxel volume, 0.14 mL; for display only, a high-pass filter was applied and the residual water peak was removed), taken from a free induction decay MRSI experiment in a grey matter location (indicated by the white arrow in the brain image inset). All assignments as in Fig. 6. SNR(NAA) is about 24 and the linewidth is 6 Hz, provided by LCModel, indicating the high sensitivity despite a voxel volume more than 10 times smaller than in Fig. 6. Courtesy of W. Bogner, Vienna, Austria.

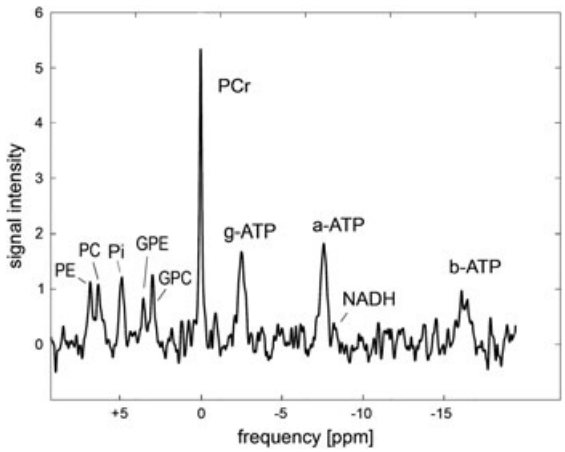

Figure 8. A localized ^{31}P spectrum from the human brain at 7 T, acquired with three-dimensional ISIS and a double-tuned 10-cm surface coil (volume of interest, $3 \times 3 \times 3\,cm^3$; acquisition time, 3 min). Note the excellent spectral resolution and sensitivity. α-ATP, α-adenosine triphosphate; β-ATP, β-adenosine triphosphate; γ-ATP, γ-adenosine triphosphate; GPC, glycerophosphocholine; GPE, glycerophosphoethanolamine; NADH, nicotinamide adenine dinucleotide, reduced form; PC, phosphatidylcholine; PCr, phosphocreatine; PE, phosphatidylethanolamine; Pi, inorganic phosphate. Courtesy of W. Bogner, Vienna, Austria.

of pathologies would manifest as bioenergetic impairment. Combining ^{1}H and ^{31}P MRSI methods with structural (diffusion tensor imaging, fibre tracking) and functional (fMRI, resting state connectivity) approaches should provide much better characterisation of complex diseases, such as epilepsy, multiple sclerosis, brain tumours, Alzheimer's disease, Parkinson's disease, and psychiatric and metabolic disorders, and allow for frequent therapy follow-ups. However, there is still much work ahead to develop and optimise robust and fast protocols at 7 T to provide clinically useful information in a reasonable examination time. Considering the slow development of novel therapies, this should not become a limiting factor.

MUSCULOSKELETAL IMAGING AT 7 T

Musculoskeletal imaging at 7 T can be divided into two main areas—morphological and compositional MRI.

Morphological MRI at 7 T

The most important structures benefiting from UHF are cartilage and trabecular bone imaging.

Cartilage imaging

Cartilage imaging at higher magnetic field strengths is expected to improve the visualisation of cartilage pathology and the segmentation of cartilage. With decreasing voxel size, partial volume effects can be reduced, which enables the measurement of cartilage volume and thickness even more reliably than with 1.5-T systems (Fig. 9). Most of the experience reported in the literature is found in cartilage imaging of the knee joint. Krug *et al.* (138) employed a voxel size of $312 \times 312 \times 1000\,\mu m^3$ in their 7-T images used for cartilage segmentation, and Regatte and Schweitzer (139) used a voxel size of $254 \times 254 \times 1000\,\mu m^3$. High-resolution images of the cartilage can be acquired not only in the knee, but also in smaller joints (e.g. in the wrist), thus improving the visualisation of cartilage interfaces (140). Fat suppression is important for accurate cartilage imaging (Fig. 10). As a result of the larger chemical shift between water and fat resonances, fat suppression is easier to achieve at 7 T than at 3 T (139).

Figure 9. Proton density-weighted fat-suppressed fast spin echo (FSE) sequence of the knee joint in the coronal plane demonstrates the cartilage layers with high resolution (at 7 T).

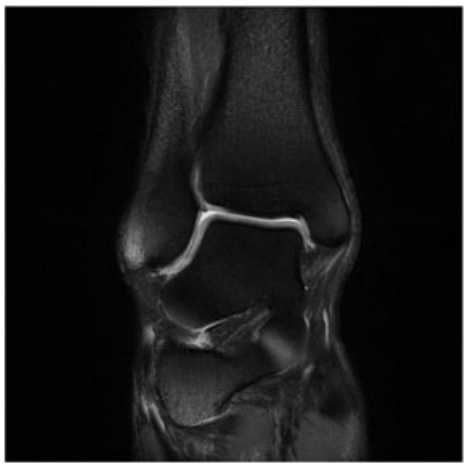

Figure 10. Proton density-weighted fat-suppressed fast spin echo (FSE) sequence of the ankle joint in the coronal plane allows the visualisation of all cartilage layers (at 7 T).

Trabecular bone imaging

It has been shown that dual X-ray measurement of bone density is not sufficient to characterise bone quality, because the trabecular bone architecture, apart from the bone density, contributes significantly to the mechanical strength, and therefore fracture risk (141,142). Such bone structure is ideally characterised by microscopic CT (143,144). However, CT cannot be used routinely *in vivo* because of the high radiation dose. *In vivo* trabecular bone imaging is one of the emerging applications for high-resolution morphological MRI. High spatial resolution is critical to visualise and quantitatively assess the morphology of trabecular bone, with the average diameter of the individual trabeculae being on the order of 100–150 μm. Regatte and Schweitzer (139), for example, were able to perform such high-resolution trabecular bone imaging at 7 T in the distal tibia using a voxel size of $156 \times 156 \times 1000\ \mu m^3$.

In comparison with 3 T, at 7 T, SNR increases by a factor of two, and thus improves the visualisation of trabecular bone structure (145). Susceptibility artefacts, caused by differences in magnetic susceptibility between trabecular bone and bone marrow, result in an artificial broadening of the trabeculae signal void, especially in gradient echo sequences (146). This effect scales with field strength and has been shown to have the advantage that it enhances the visibility of small trabeculae which would otherwise disappear because of the partial volume effect (138). Krug *et al*. (10) were able to demonstrate high correlations between 3-T and 7-T MRI, as well as between MRI and high-resolution CT, with regard to the apparent trabecular bone number. For most of the other structural bone parameters, including bone fraction, trabecular spacing and the number of trabeculae, high correlations were also found between 3-T and 7-T MRI.

Clinical applications

It should be noted that, for many indications, it is not yet clear whether improved image quality also increases diagnostic accuracy. UHF MR images might further enhance our diagnostic confidence in the future. However, based on our current experience, it is unlikely that the diagnostic accuracy for these conditions, considering morphological imaging alone (without additional functional imaging), will be increased substantially with the transition from 3 to 7 T. For these and other common indications, where diagnostic accuracy is already high at 1.5 T, the relative advantage of 3 T or above might be to shorten the acquisition time whilst maintaining an equivalent level of contrast and resolution, or to combine information from morphological and functional imaging, still keeping the total examination time constant.

Knee imaging

Chang *et al*. (147) performed the first *in vivo* 7-T MRI study of the knee. These authors investigated trabecular bone microarchitecture and detected activity-related changes in Olympic fencers when compared with healthy controls.

Other authors have used 7 T for the morphological assessment of articular cartilage and have reported up to a 2.4-fold increase in SNR compared with that obtained at 3 T (10). One study detected an increase in SNR from 3 to 7 T that was significant only for gradient echo sequences, but not for TSE sequences (148). As a result of SAR limitations, scan parameters for the TSE sequence had to be modified, which resulted in an incomplete coverage of the knee joint, extensive artefacts and poor fat saturation. The contrast-to-noise ratio and image quality were increased for the gradient echo sequences, but decreased for the TSE sequences. Comparing 3 and 7 T, the level of confidence for the diagnosis of cartilage lesions was higher in the gradient echo and lower in the TSE sequences; however, overall, the TSE sequences at 3 T had the highest confidence score. The evaluation of bone marrow oedema was decreased at 7 T because of the limited performance of the TSE sequence.

Kraff *et al*. (149) performed a comparison between knee imaging at 1.5 and 7 T, and also reported that, because of the SAR limitations with the FSE sequences, successive measurements were needed for complete coverage of the knee joint. They also confirmed that bone marrow oedema was better visualised at 1.5 T than at 7 T.

Currently, no study has verified a statistically significant increase in diagnostic accuracy for the detection of common pathologies in the knee when moving to MR scanners with field strengths above 3 T. FSE sequences are widely used in musculoskeletal imaging; however, because of the number of 180° RF pulses, FSE techniques suffer from high SAR, which easily exceeds the exposure limits. This results in a small number of slices, which does not allow coverage of the entire joint within one scan.

Compositional MR at 7 T

Collagen fibre- and water-specific techniques

T_2 relaxation time mapping of articular cartilage at UHFs. The transverse relaxation time constant (T_2) of cartilage is a sensitive parameter for the evaluation of changes in water and collagen content and tissue anisotropy (150). Cartilage T_2 reflects the interaction of water and the extracellular matrix on a molecular level. The collagen fibre orientation defines the layers of articular cartilage. In healthy articular cartilage, an increase in T_2 values from the deep to superficial cartilage layers can be observed, based on the anisotropy of collagen fibres running perpendicular to cortical bone in the deep layer of cartilage (151). Different cartilage locations (patella, femur and tibia) were evaluated in one study by Welsch *et al*. (152) at 7 T using multi-echo spin echo T_2 mapping, and showed results comparable with those of Pakin *et al*. (153), with a significant decrease in T_2 values between femoral and tibial weight-bearing cartilage. Furthermore, the patella showed lower T_2 values than the femoral condyle (Fig. 11). In cartilage repair tissue, global (bulk, full-thickness) T_2 and, especially, zonal T_2 evaluations have shown very promising results. Comparable with the results at 3 T, 7-T multi-echo spin echo T_2 mapping could also be used for the assessment of patients after cartilage repair (152), and may provide higher resolution within the same scan time compared with 3 T.

T_2 relaxation time mapping of articular cartilage at UHFs.* In addition to standard spin echo T_2 mapping, T_2*-weighted three-dimensional gradient echo articular cartilage mapping has shown reliable results in the evaluation of osteoarthritic cartilage changes of the knee (154). In recent studies, T_2* mapping, with short scan times, was correlated with standard spin echo T_2, and provided information comparable with that obtained for articular cartilage using spin echo T_2, but with overall lower T_2* values (155,156). Furthermore, also for T_2*, a clear zonal variation between the deep and superficial cartilage layers was described for healthy cartilage.

Proteoglycan (PG)-specific techniques

^{23}Na MRI: background and basic findings. Articular cartilage consists mainly of an extracellular matrix made up of type II collagen, PG, chondrocytes and water (157). PG consists of a linear protein core to which many glycoproteins, known as glycosaminoglycans (GAGs) (158), are attached. PG serves to cross-link the collagen fibrils in the extracellular matrix to provide both compressive and tensile strength to the matrix. The sulphate and carboxyl groups of GAG impart a negative fixed charge density (FCD) to the matrix. These negative ions attract positive counter-ions (sodium) and water molecules, and provide osmotic and electrostatic forces, which are responsible for the swelling pressure of cartilage. This partly explains the importance of GAG for the biomechanical properties of articular cartilage. The loss of PG from the extracellular matrix has been reported to be the event that initiates the onset of osteoarthritis (159,160) and a reduction in FCD in the cartilage. Maroudas *et al*. (161) have shown that the FCD of cartilage is correlated with the GAG content. As the FCD is counter-balanced by sodium ions, the loss of PG (and hence GAG and FCD) as a result of cartilage degeneration results in the loss of sodium ions from the tissue. Based on these mechanisms, ^{23}Na MRI has been validated as a quantitative method of computing FCD, and hence PG content, in healthy humans (162–164).

Clinical application of sodium imaging. ^{23}Na MRI experiments have been performed on the knee cartilage of healthy subjects and patients with early-stage osteoarthritis at 4 T, and have demonstrated the feasibility of ^{23}Na MRI in computing PG loss in the early stage. The major advantage of ^{23}Na MRI, especially of cartilage, is that it is highly specific for PG content. As the sodium from surrounding structures in the joint is low (<50 mM), cartilage can be visualised with very high contrast without the requirement for any exogenous contrast agent, such as that required in delayed gadolinium-enhanced MRI of cartilage (dGEMRIC) (165). It can be used to quantify early molecular changes in osteoarthritis.

The disadvantages of ^{23}Na MRI are that it requires field strengths of more than 3 T to obtain quality sodium images that enable the accurate quantification of cartilage FCD. As the fast T_2 decay of cartilage ranges between 1 and 2 ms, substantial signal loss occurs before data acquisition. In addition, the MR sensitivity for ^{23}Na is only 9.2% of the ^{1}H MR sensitivity, and the *in vivo* concentration is approximately 360 times lower than the *in vivo* water proton concentration. The combination of these factors results in a ^{23}Na signal that is approximately 4000 times smaller than the corresponding ^{1}H signal.

However, as for human joints, SNR scales linearly with B_0 (4,166,167) and, because of the much longer wavelength of ^{23}Na relative to ^{1}H, sodium imaging does not suffer from B_1 interference and penetration or the B_0 susceptibility problems

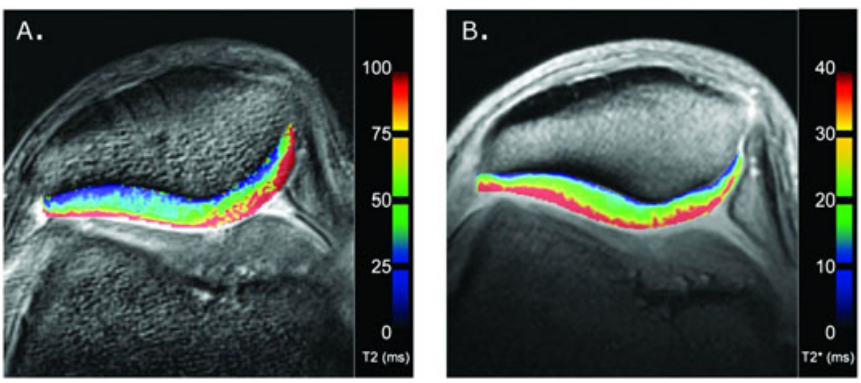

Figure 11. T_2 (a) and T_2* (b) mapping of the patella in the axial plane visualises the zonal variation of cartilage based on the collagen fibre network in articular cartilage (at 7 T).

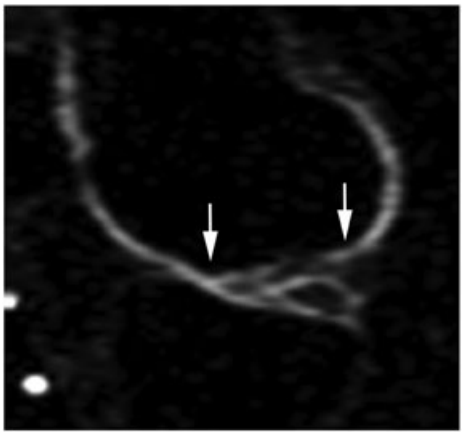

Figure 12. Sodium image in the sagittal plane shows an area of cartilage transplantation with inhomogeneously lower sodium signal in the repair tissue, corresponding to lower glycosaminoglycan content (white arrows mark the borders of the transplant).

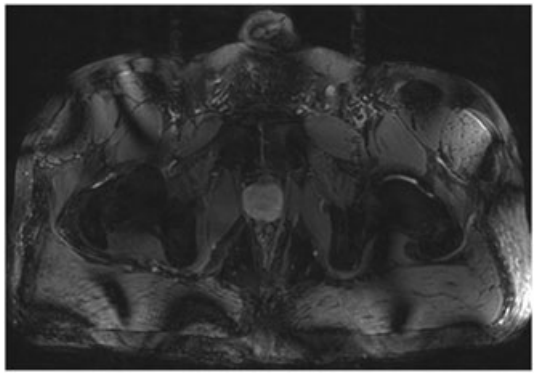

Figure 13. Turbo spin echo image at 7 T revealing severe artefacts as a result of inhomogeneities in the transmit B_1^+ radiofrequency field.

experienced in proton imaging. Therefore, ^{23}Na MRI is particularly advantageous at higher field, in particular at 7 T. Further, unlike proton T_1, which increases with field strength, the T_1 of sodium is governed predominantly by quadrupolar interaction, and may not change appreciably at higher fields. This retains the rapid averaging capability of ^{23}Na MRI, even at high fields. The low gyromagnetic ratio of sodium also leads to significantly lower power deposition relative to proton imaging. Although ^{23}Na MRI has high specificity and does not require any exogenous contrast agent, it does require special hardware capabilities (multinuclear), specialised RF coils (transmit–receive) and, most probably, three-dimensional ultrashort TE sequences.

Recently, sodium imaging has been applied to patients after matrix-associated autologous transplantation. Using a 7-T whole-body system and a modified three-dimensional gradient echo sequence, a sufficiently high SNR of 24 (range, 17–30) in native cartilage allowed the visualisation of even the femoral condyle cartilage layer. This layer is thinner than the patellar cartilage, but is the preferred location for cartilage transplantation. Reports on sodium imaging of the knee joint have, to date, focused on the patellar cartilage layer. In the patient group, sodium imaging allowed the discrimination between different concentrations of sodium, which correlated with the GAG content in transplants, as compared with native, healthy cartilage (Fig. 12). The mean normalised sodium values were 125 mM (range, 72–244) for the repair tissue within the cartilage transplant and 192 mM (range, 98–259) for healthy cartilage. A good correlation between sodium imaging and dGEMRIC, another PG-specific method for the quantification of GAG concentration in patients after matrix-associated autologous transplantation, was found (28).

BODY IMAGING AT 7 T

One of the most prominent technical hindrances to the clinical application of 7 T outside the brain and extremities is uneven RF penetration and the consequent inhomogeneous excitation of the body tissue. RF inhomogeneity is particularly problematic in anatomical regions with large cross-sections (Fig. 13). Therefore, it can be expected that the first clinical applications of 7 T will target the head or extremities, but technological solutions for body imaging at 7 T are being actively pursued, and initial results indicate that the future application of 7 T, even in the torso, will be viable, as is already the case at 1.5 and 3 T.

What improvements in whole-body clinical diagnosis can be expected at 7 T? Although the answer to this question remains open because of the nascent state of research in this area, one can expect that advantages will be pursued utilising similar strategies to those employed in brain and musculoskeletal imaging: higher spatial resolution; improved spectroscopy and spectroscopic imaging, both for hydrogen and other nuclei; extraction of additional information from the image phase; and new or improved tissue contrasts, particularly those related to magnetic susceptibility.

Initial research within the thorax and abdomen has centred around the pursuit of technical solutions to help alleviate RF inhomogeneities and demonstrate basic imaging feasibility (57,168). This work generally involves multichannel transmit coils and the use of either static or dynamic RF shimming of the B_1^+ transmit field (43,169). In addition, new acquisition strategies have been proposed which combine the data acquired with two or more independent RF shims with complementary B_1^+ field patterns to achieve improved overall homogeneity (170).

Figure 14a depicts a multichannel coil based on stripline elements (171,172). With this coil, the eight elements can be controlled independently of each other during tissue excitation. Thus, a significant improvement in excitation uniformity and coverage can be reached (Fig. 14b). This work was conducted in healthy volunteers, and patient investigations are still outstanding. However, even these early imaging results demonstrate the successful transformation of the increased SNR into a high spatiotemporal resolution, yielding highly defined anatomical depiction and confirming the expected improved performance of parallel imaging (173–175). Nevertheless, the impact of enhanced structural resolution on diagnostic performance still remains to be determined.

In particular, non-enhanced angiographic applications in the abdomen appear to be promising, as the high signal intensity of the hepatic or renal vasculature provides excellent conspicuity of the vessels. The potential for robust vascular imaging without contrast agent is attractive because of the lower cost and data linking nephrogenic systemic fibrosis to gadolinium contrast agent exposure (176). The inherently positive vessel to background contrast at 7 T in various gradient echo sequences, regardless of image orientation, has also been observed in the

a)

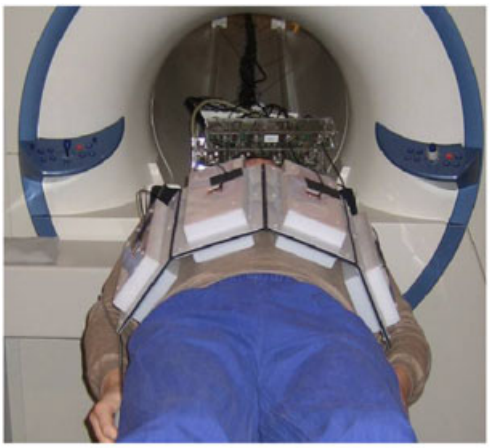

b)

Figure 14. (a) A 7-T eight-channel body array composed of four anterior and four posterior stripline elements. (b) By applying complex weightings to the excitation pulses on each channel (radiofrequency shimming), a significant improvement in excitation uniformity and image quality can be achieved, but residual inhomogeneities remain.

brain (94,98). The aetiology of the high vascular signal intensity at 7 T remains partially unresolved, as inflow as well as steady-state effects seem to be accountable. As a result of the utilisation of local transmit–receive RF coils at 7 T, flowing spins are not presaturated by non-selective RF pulses before they enter the imaging region. Hence, the impact of inflowing 'fresh' spins to the hyperintense blood signal may be greater than with an extended body transmit coil (177).

Cardiac imaging is also of intense interest at 7 T (178). The hyperintense blood pool in spoiled gradient echo sequences is particularly advantageous for wall function studies of the heart (168,179,180). Although balanced steady-state free precession sequences (e.g. true fast imaging with steady-state precession, fast imaging employing steady-state acquisition or balanced fast field echo) represent the state of the art for wall motion studies at lower field strengths and demonstrate outstanding performance at 1.5 T, such balanced steady-state free precession sequences are severely compromised at 7 T by contrast loss (myocardium to blood), dark banding artefacts caused by off-resonance effects and generally severe signal inhomogeneities. In addition, SAR restrictions inhibit the utilisation of a suitably high excitation flip angle. Cine spoiled gradient echo sequences (e.g. FLASH, spoiled gradient recalled or fast field echo), however, provide suitable imaging quality with good signal homogeneity over almost the entire cardiac volume, and good myocardium to blood contrast (Fig. 15).

A clear weakness of cardiac imaging at 1.5 T, and even at 3 T, is the unreliable depiction of the coronary arteries. At 7 T, it should be theoretically possible to further improve the spatial resolution and thus resolve the fine details of these very small structures. Initial coronary imaging at 7 T has been demonstrated, but there are still many technical challenges to be addressed before image quality is competitive with either 1.5 or 3 T (181,182). In addition to other challenges, respiratory and cardiac triggering is vital to compensate for physiological motion during any type of cardiac study. At 7 T, ECG triggering functions quite poorly because of the elevated T wave and other interferences (183). An alternative, which has been pursued to side step this issue, is to use acoustic rather than electrical-based triggering (184,185).

For diseases of the central nervous system, examination of the spinal cord and column is critical. Particularly for the spinal cord, the advantages of 7 T which have been identified in the brain can be expected to be transferable. Several groups have introduced dedicated coils for examining the spinal column, including a design consisting of eight non-overlapping microstrip loop elements (186), a design with two columns of four overlapping loops each (187) and a coil with dedicated quadrature transmit and eight-channel receive (188). With these coils, large field of view acquisitions, utilising multichannel transmit and parallel receive with reduction factors of four, are achievable.

One organ that has been targeted very early at 7 T is the prostate (189,190). It is very challenging to grade the aggressiveness of prostate carcinoma, even at 3 T. With the broad application of blood screening tests based on the serum level of prostate-specific antigen, the early detection of prostate cancer has been improved significantly. However, the specificity of the prostate-specific antigen test is very low, as benign prostate inflammation leads to many false positive results, and many of the detected

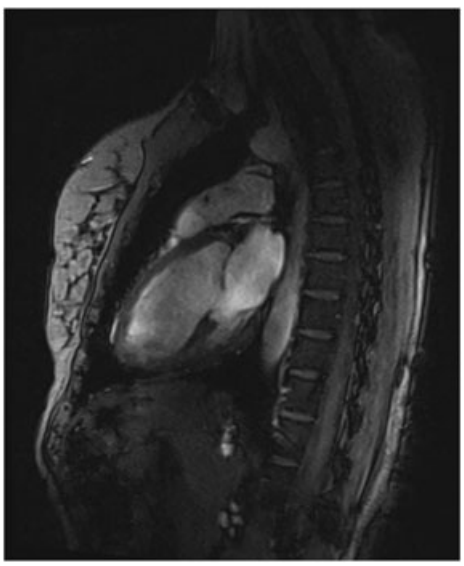

Figure 15. Long-axis cine spoiled gradient echo (fast low-angle shot, FLASH) image acquired at 7 T with a multichannel transmit coil and radiofrequency shimming. The myocardium to blood contrast at 7 T is superior *versus* lower field strengths, making spoiled gradient echo an alternative to balanced steady-state free precession for cardiac functional studies.

cancers are not aggressive and could be left untreated to avoid the risks and side-effects of treatment. It is hoped that MRI and MRS or MRSI at 7 T will improve the characterisation and staging of prostate cancers. Initial work has demonstrated ^{1}H MRSI with voxel sizes down to 3.5 mm^3, significantly reducing partial volume effects, and the optimised detection of polyamines for the enhancement of specificity (190,191). Two recent studies in the prostate have compared the application of external coil arrays *versus* endorectal coils (192,193).

Finally, imaging of the female breast has been pursued at 7 T (194–196). A continuing challenge for clinical MR breast imaging is its relatively low specificity, and 7 T could help address this issue, in particular in conjunction with spectroscopic techniques (197).

CONCLUSIONS

In spite of the challenges encountered when moving to 7 T, the rapid development in this research field shows that new technical solutions may overcome many of the obstacles discussed.

The steadily increasing installation of UHF MR scanners during the last few years has demonstrated that extended use of 7 T, at least in clinical research, is now becoming a reality. One example is the first clinical study on the use of sodium imaging at 7 T to evaluate the quality of repair tissue after cartilage repair surgery. Another example is the first clinical comparison of presurgical localisation of the primary hand area in patients with tumours, revealing a significantly higher functional sensitivity at 7 T relative to 3 T. ^{1}H and ^{31}P MRSI, in addition to helping to improve our understanding of basic neurochemical mechanisms in the human brain, should provide deeper insights into the pathogenesis of major neurological and psychiatric diseases, as well as muscle deficiencies, and, in this way, further improve the diagnostic specificity. In addition, it has been shown that parallel imaging can be utilised with higher speed reduction factors at higher field strengths, significantly reducing the acquisition time. Moreover, parallel transmission MR should alleviate problems caused by inhomogeneous excitation; however, substantial research work is required with respect to patient safety calculations (B_1, SAR, etc.) before parallel transmit technology can be used routinely.

The research potential described above, in our opinion, is unquestionable, and will most probably result in the establishment of more than 50 systems worldwide during the next few years. Furthermore, technical demands on staff are expected to be reduced significantly in parallel with the technical developments and extended clinical availability. We therefore foresee an extended use of 7 T as a platform for clinically oriented research. Provided that regulatory issues are handled, clinical research results may well pave the way for 7 T to become a clinical diagnostic tool of significant potential in the future.

Acknowledgements

EM and ST are supported via an unlimited research grant from Siemens Healthcare (Erlangen, Germany) and the Austrian Science Fund (FWF). ST acknowledges the Vienna Spots of Excellence Programme. ML would like to thank Professor Elke R. Gizewski (Department of Neuroradiology, University Hospital Giessen, Germany) and Professor Dagmar Timman-Braun (Department of Neurology, University Hospital Essen, Germany) for the many constructive conversations supporting this work. FS acknowledges the Swedish Research Council and the Knut and Alice Wallenberg Foundation.

REFERENCES

1. Moser E, Trattnig S. 3.0 Tesla MR systems. Invest. Radiol. 2003; 38(7): 375–376.
2. Robitaille PM, Abduljalil AM, Kangarlu A. Ultra high resolution imaging of the human head at 8 tesla: 2K x 2K for Y2K. J. Comput. Assist. Tomogr. 2000; 24(1): 2–8.
3. Vaughan JT, Garwood M, Collins CM, Liu W, DelaBarre L, Adriany G, Andersen P, Merkle H, Goebel R, Smith MB, Ugurbil K. 7 T vs. 4 T: RF power, homogeneity, and signal-to-noise comparison in head images. Magn. Reson. Med. 2001; 46(1): 24–30.
4. Ugurbil K, Adriany G, Andersen P, Chen W, Garwood M, Gruetter R, Henry PG, Kim SG, Lieu H, Tkac I, Vaughan T, Van De Moortele PF, Yacoub E, Zhu XH. Ultrahigh field magnetic resonance imaging and spectroscopy. Magn. Reson. Imaging 2003; 21(10): 1263–1281.
5. Norris DG. High field human imaging. J. Magn. Reson. Imaging 2003; 18(5): 519–529.
6. Tkac I, Andersen P, Adriany G, Merkle H, Ugurbil K, Gruetter R. In vivo ^{1}H NMR spectroscopy of the human brain at 7 T. Magn. Reson. Med. 2001; 46(3): 451–456.
7. Yacoub E, Shmuel A, Pfeuffer J, Van De Moortele PF, Adriany G, Andersen P, Vaughan JT, Merkle H, Ugurbil K, Hu X. Imaging brain function in humans at 7 Tesla. Magn. Reson. Med. 2001; 45(4): 588–594.
8. Pfeuffer J, Adriany G, Shmuel A, Yacoub E, Van De Moortele PF, Hu X, Ugurbil K. Perfusion-based high-resolution functional imaging in the human brain at 7 Tesla. Magn. Reson. Med. 2002; 47(5): 903–911.
9. Terpstra M, Ugurbil K, Gruetter R. Direct in vivo measurement of human cerebral GABA concentration using MEGA-editing at 7 Tesla. Magn. Reson. Med. 2002; 47(5): 1009–1012.
10. Krug R, Carballido-Gamio J, Banerjee S, Burghardt AJ, Link TM, Majumdar S. In vivo ultra-high-field magnetic resonance imaging of trabecular bone microarchitecture at 7 T. J. Magn. Reson. Imaging 2008; 27(4): 854–859.
11. Kollia K, Maderwald S, Putzki N, Schlamann M, Theysohn JM, Kraff O, Ladd ME, Forsting M, Wanke I. First clinical study on ultra-high-field MR imaging in patients with multiple sclerosis: comparison of 1.5 T and 7 T. Am. J. Neuroradiol. 2009; 30(4): 699–702.
12. Laule C, Kozlowski P, Leung E, Li DK, Mackay AL, Moore GR. Myelin water imaging of multiple sclerosis at 7 T: correlations with histopathology. Neuroimage 2008; 40(4): 1575–1580.
13. Nakada T, Matsuzawa H, Igarashi H, Fujii Y, Kwee IL. In vivo visualization of senile-plaque-like pathology in Alzheimer's disease patients by MR microscopy on a 7 T system. J. Neuroimaging 2008; 18(2): 125–129.
14. Yao B, Li TQ, Gelderen P, Shmueli K, de Zwart JA, Duyn JH. Susceptibility contrast in high field MRI of human brain as a function of tissue iron content. NeuroImage 2009; 44(4): 1259–1266.
15. Triantafyllou C, Hoge RD, Krueger G, Wiggins CJ, Potthast A, Wiggins GC, Wald LL. Comparison of physiological noise at 1.5 T, 3 T and 7 T and optimization of fMRI acquisition parameters. Neuroimage 2005; 26(1): 243–250.
16. van der Zwaag W, Francis S, Head K, Peters A, Gowland P, Morris P, Bowtell R. fMRI at 1.5, 3 and 7 T: characterising BOLD signal changes. Neuroimage 2009; 47(4): 1425–1434.
17. Reichenbach JR, Barth M, Haacke EM, Klarhofer M, Kaiser WA, Moser E. High-resolution MR venography at 3.0 Tesla. J. Comput. Assist. Tomogr. 2000; 24(6): 949–957.
18. Deistung A, Rauscher A, Sedlacik J, Stadler J, Witoszynskyj S, Reichenbach JR. Susceptibility weighted imaging at ultra high magnetic field strengths: theoretical considerations and experimental results. Magn. Reson. Med. 2008; 60(5): 1155–1168.
19. Reichenbach JR, Venkatesan R, Schillinger DJ, Kido DK, Haacke EM. Small vessels in the human brain: MR venography with deoxyhemoglobin as an intrinsic contrast agent. Radiology 1997; 204(1): 272–277.
20. Schweser F, Deistung A, Lehr BW, Reichenbach JR. Quantitative imaging of intrinsic magnetic tissue properties using MRI signal phase: an approach to in vivo brain iron metabolism? NeuroImage 2011; 54(4): 2789–2807.

21. de Rochefort L, Brown R, Prince MR, Wang Y. Quantitative MR susceptibility mapping using piece-wise constant regularized inversion of the magnetic field. Magn. Reson. Med. 2008; 60(4): 1003–1009.
22. Schweser F, Deistung A, Lehr BW, Reichenbach JR. Differentiation between diamagnetic and paramagnetic cerebral lesions based on magnetic susceptibility mapping. Med. Phys. 2010; 37(10): 5165–5178.
23. Haacke EM, Tang J, Neelavalli J, Cheng YC. Susceptibility mapping as a means to visualize veins and quantify oxygen saturation. J. Magn. Reson. Imaging 2010; 32(3): 663–676.
24. Li W, Wu B, Liu C. Quantitative susceptibility mapping of human brain reflects spatial variation in tissue composition. NeuroImage 2011; 55(4): 1645–1656.
25. Jerde TA, Lewis SM, Goerke U, Gourtzelidis P, Tzagarakis C, Lynch J, Moeller S, Van de Moortele PF, Adriany G, Trangle J, Ugurbil K, Georgopoulos AP. Ultra-high field parallel imaging of the superior parietal lobule during mental maze solving. Exp. Brain Res. 2008; 187(4): 551–561.
26. Scheenen TW, Heerschap A, Klomp DW. Towards ^{1}H-MRSI of the human brain at 7 T with slice-selective adiabatic refocusing pulses. MAGMA 2008; 21(1–2): 95–101.
27. Hussain MS, Stobbe RW, Bhagat YA, Emery D, Butcher KS, Manawadu D, Rizvi N, Maheshwari P, Scozzafava J, Shuaib A, Beaulieu C. Sodium imaging intensity increases with time after human ischemic stroke. Ann. Neurol. 2009; 66(1): 55–62.
28. Trattnig S, Welsch GH, Juras V, Szomolanyi P, Mayerhoefer ME, Stelzeneder D, Mamisch TC, Bieri O, Scheffler K, Zbyn S. ^{23}Na MR imaging at 7 T after knee matrix-associated autologous chondrocyte transplantation preliminary results. Radiology 2010; 257(1): 175–184.
29. Cady EB. *Clinical Magnetic Resonance Spectroscopy*. Plenum Press: New York and London; 1990.
30. Moser E. Ultra-high field magnetic resonance: why and when? World J. Radiol. 2010; 2(2): 4.
31. Moser E, Meyerspeer M, Fischmeister FPS, Grabner G, Bauer H, Trattnig S. Windows on the human body—in vivo high-field magnetic resonance research and applications in medicine and psychology. Sensors 2010; 10(6): 33.
32. Rooney WD, Johnson G, Li X, Cohen ER, Kim SG, Ugurbil K, Springer CS, Jr. Magnetic field and tissue dependencies of human brain longitudinal $^{1}H_2O$ relaxation in vivo. Magn. Reson. Med. 2007; 57(2): 308–318.
33. Bogner W, Chmelik M, Schmid AI, Moser E, Trattnig S, Gruber S. Assessment of (31)P relaxation times in the human calf muscle: a comparison between 3 T and 7 T in vivo. Magn. Reson. Med. 2009; 62(3): 574–582.
34. Meyerspeer M, Kemp GJ, Mlynarik V, Krssak M, Szendroedi J, Nowotny P, Roden M, Moser E. Direct noninvasive quantification of lactate and high energy phosphates simultaneously in exercising human skeletal muscle by localized magnetic resonance spectroscopy. Magn. Reson. Med. 2007; 57(4): 654–660.
35. Meyerspeer M, Scheenen T, Mandl Th, Unger E, Moser E. Semi-LASER localized dynamic ^{31}P MRS in exercising muscle at ultra-high magnetic field. Magn. Reson. Med. 2010; 65(5): 1207–1215.
36. Ladd ME. High-field-strength magnetic resonance: potential and limits. Top. Magn. Reson. Imaging 2007; 18(2): 139–152.
37. Adriany G, Van de Moortele PF, Wiesinger F, Moeller S, Strupp JP, Andersen P, Snyder C, Zhang X, Chen W, Pruessmann KP, Boesiger P, Vaughan T, Ugurbil K. Transmit and receive transmission line arrays for 7 Tesla parallel imaging. Magn. Reson. Med. 2005; 53(2): 434–445.
38. Wiesinger F, Boesiger P, Pruessmann KP. Electrodynamics and ultimate SNR in parallel MR imaging. Magn. Reson. Med. 2004; 52(2): 376–390.
39. Wiesinger F, Van de Moortele PF, Adriany G, De Zanche N, Ugurbil K, Pruessmann KP. Potential and feasibility of parallel MRI at high field. NMR Biomed. 2006; 19(3): 368–378.
40. Brunner DO, De Zanche N, Frohlich J, Paska J, Pruessmann KP. Travelling-wave nuclear magnetic resonance. Nature 2009; 457 (7232): 994–998.
41. Van de Moortele PF, Akgun C, Adriany G, Moeller S, Ritter J, Collins CM, Smith MB, Vaughan JT, Ugurbil K. B(1) destructive interferences and spatial phase patterns at 7 T with a head transceiver array coil. Magn. Reson. Med. 2005; 54(6): 1503–1518.
42. Setsompop K, Alagappan V, Zelinski AC, Potthast A, Fontius U, Hebrank F, Schmitt F, Wald LL, Adalsteinsson E. High-flip-angle slice-selective parallel RF transmission with 8 channels at 7 T. J. Magn. Reson. 2008; 195(1): 76–84.
43. Katscher U, Bornert P. Parallel RF transmission in MRI. NMR Biomed. 2006; 19(3): 393–400.
44. Katscher U, Bornert P, Leussler C, van den Brink JS. Transmit SENSE. Magn. Reson. Med. 2003; 49(1): 144–150.
45. Heidemann RM, Porter DA, Anwander A, Feiweier T, Heberlein K, Knosche TR, Turner R. Diffusion imaging in humans at 7 T using readout-segmented EPI and GRAPPA. Magn. Reson. Med. 2010; 64(1): 9–14.
46. Blamire AM, Rothman DL, Nixon T. Dynamic shim updating: a new approach towards optimized whole brain shimming. Magn. Reson. Med. 1996; 36(1): 159–165.
47. Sengupta S, Welch EB, Zhao Y, Foxall D, Starewicz P, Anderson AW, Gore JC, Avison MJ. Dynamic B(0) shimming at 7 T. Magn. Reson. Imaging 2011; 29(4): 483–496.
48. Henning A, Fuchs A, Murdoch JB, Boesiger P. Slice-selective FID acquisition, localized by outer volume suppression (FIDLOVS) for (1)H-MRSI of the human brain at 7 T with minimal signal loss. NMR Biomed. 2009; 22(7): 683–696.
49. Hetherington HP, Avdievich NI, Kuznetsov AM, Pan JW. RF shimming for spectroscopic localization in the human brain at 7 T. Magn. Reson. Med. 2010; 63(1): 9–19.
50. Avdievich NI, Pan JW, Baehring JM, Spencer DD, Hetherington HP. Short echo spectroscopic imaging of the human brain at 7 T using transceiver arrays. Magn. Reson. Med. 2009; 62(1): 17–25.
51. Balchandani P, Spielman D. Fat suppression for ^{1}H MRSI at 7 T using spectrally selective adiabatic inversion recovery. Magn. Reson. Med. 2008; 59(5): 980–988.
52. Xu D, Cunningham CH, Chen AP, Li Y, Kelley DA, Mukherjee P, Pauly JM, Nelson SJ, Vigneron DB. Phased array 3D MR spectroscopic imaging of the brain at 7 T. Magn. Reson. Imaging 2008; 26(9): 1201–1206.
53. Schuster C, Dreher W, Stadler J, Bernarding J, Leibfritz D. Fast three-dimensional ^{1}H MR spectroscopic imaging at 7 Tesla using 'spectroscopic missing pulse—SSFP'. Magn. Reson. Med. 2008; 60(5): 1243–1249.
54. Wright AC, Lemdiasov R, Connick TJ, Bhagat YA, Magland JF, Song HK, Toddes SP, Ludwig R, Wehrli FW. Helmholtz-pair transmit coil with integrated receive array for high-resolution MRI of trabecular bone in the distal tibia at 7 T. J. Magn. Reson. 2011; 210(1): 113–122.
55. Zelinski AC, Angelone LM, Goyal VK, Bonmassar G, Adalsteinsson E, Wald LL. Specific absorption rate studies of the parallel transmission of inner-volume excitations at 7 T. J. Magn. Reson. Imaging 2008; 28(4): 1005–1018.
56. van den Bergen B, van den Berg CA, Klomp DW, Lagendijk JJ. SAR and power implications of different RF shimming strategies in the pelvis for 7 T MRI. J. Magn. Reson. Imaging 2009; 30(1): 194–202.
57. Vaughan JT, Snyder CJ, DelaBarre LJ, Bolan PJ, Tian J, Bolinger L, Adriany G, Andersen P, Strupp J, Ugurbil K. Whole-body imaging at 7 T: preliminary results. Magn. Reson. Med. 2009; 61(1): 244–248.
58. Chakeres DW, Kangarlu A, Boudoulas H, Young DC. Effect of static magnetic field exposure of up to 8 Tesla on sequential human vital sign measurements. J. Magn. Reson. Imaging 2003; 18(3): 346–352.
59. de Vocht F, Stevens T, Glover P, Sunderland A, Gowland P, Kromhout H. Cognitive effects of head-movements in stray fields generated by a 7 Tesla whole-body MRI magnet. Bioelectromagnetics 2007; 28(4): 247–255.
60. Theysohn JM, Maderwald S, Kraff O, Moenninghoff C, Ladd ME, Ladd SC. Subjective acceptance of 7 Tesla MRI for human imaging. MAGMA 2008; 21(1–2): 63–72.
61. International Electrotechnical Commission (IEC). Medical electrical equipment–Particular requirements for the safety of magnetic resonance equipment for medical diagnosis. *IEC 60601-2-33, 3.0 2010–03 edn*. International Electrotechnical Commission: Geneva, Switzerland; 2010.
62. International Commission on Non-Ionizing Radiation Protection (ICNIRP). Guidelines on limits of exposure to static magnetic fields. Health Phys. 2009; 96(4): 504–514.
63. International Commission on Non-Ionizing Radiation Protection (ICNIRP). Guidelines for limiting exposure to time-varying electric and magnetic fields (1 Hz to 100 kHz). Health Phys. 2010; 99(6): 818–836.

64. Moser E, Trattnig S. Institute Spotlight. Diagnostic Imaging Europe 2011; February/March: 16–18.
65. Lupo JM, Banerjee S, Hammond KE, Kelley DA, Xu D, Chang SM, Vigneron DB, Majumdar S, Nelson SJ. GRAPPA-based susceptibility-weighted imaging of normal volunteers and patients with brain tumor at 7 T. Magn. Reson. Imaging 2009; 27(4): 480–488.
66. Moenninghoff C, Maderwald S, Theysohn JM, Kraff O, Ladd ME, El Hindy N, van de Nes J, Forsting M, Wanke I. Imaging of adult astrocytic brain tumours with 7 T MRI: preliminary results. Eur. Radiol. 2009; 20(3): 704–713.
67. Monninghoff C, Maderwald S, Theysohn JM, Schutt P, Gauler T, Kraff O, Ladd ME, Ladd SC, Wanke I. Imaging of brain metastases of bronchial carcinomas with 7 T MRI—initial results. Rofo 2010; 182(9): 764–772.
68. Theysohn JM, Kraff O, Maderwald S, Schlamann MU, de Greiff A, Forsting M, Ladd SC, Ladd ME, Gizewski ER. The human hippocampus at 7 T—in vivo MRI. Hippocampus 2009; 19(1): 1–7.
69. Thomas BP, Welch EB, Niederhauser BD, Whetsell WO Jr, Anderson AW, Gore JC, Avison MJ, Creasy JL. High-resolution 7 T MRI of the human hippocampus in vivo. J. Magn. Reson. Imaging 2008; 28(5): 1266–1272.
70. Zijlmans M, de Kort GA, Witkamp TD, Huiskamp GM, Seppenwoolde JH, van Huffelen AC, Leijten FS. 3 T versus 1.5 T phased-array MRI in the presurgical work-up of patients with partial epilepsy of uncertain focus. J. Magn. Reson. Imaging 2009; 30(2): 256–262.
71. Breyer T, Wanke I, Maderwald S, Woermann FG, Kraff O, Theysohn JM, Ebner A, Forsting M, Ladd ME, Schlamann M. Imaging of patients with hippocampal sclerosis at 7 Tesla: initial results. Acad. Radiol. 2010; 17(4): 421–426.
72. Cho ZH, Han JY, Hwang SI, Kim DS, Kim KN, Kim NB, Kim SJ, Chi JG, Park CW, Kim YB. Quantitative analysis of the hippocampus using images obtained from 7.0 T MRI. Neuroimage 2010; 49(3): 2134–2140.
73. Cho ZH, Kim YB, Han JY, Kim NB, Hwang SI, Kim SJ, Cho SJ. Altered T2* relaxation time of the hippocampus in major depressive disorder: implications of ultra-high field magnetic resonance imaging. J. Psychiatr. Res. 2010; 44(14): 881–886.
74. Meyer JS, Quach M, Thornby J, Chowdhury M, Huang J. MRI identifies MCI subtypes: vascular versus neurodegenerative. J. Neurol. Sci. 2005; 229–230: 121–129.
75. Visser F, Zwanenburg JJ, Hoogduin JM, Luijten PR. High-resolution magnetization-prepared 3D-FLAIR imaging at 7.0 Tesla. Magn. Reson. Med. 2010; 64(1): 194–202.
76. Zwanenburg JJ, Hendrikse J, Visser F, Takahara T, Luijten PR. Fluid attenuated inversion recovery (FLAIR) MRI at 7.0 Tesla: comparison with 1.5 and 3.0 Tesla. Eur. Radiol. 2010; 20(4): 915–922.
77. Werring DJ, Frazer DW, Coward LJ, Losseff NA, Watt H, Cipolotti L, Brown MM, Jager HR. Cognitive dysfunction in patients with cerebral microbleeds on T2*-weighted gradient-echo MRI. Brain 2004; 127(Pt 10): 2265–2275.
78. Derex L, Nighoghossian N, Hermier M, Adeleine P, Philippeau F, Honnorat J, Yilmaz H, Dardel P, Froment JC, Trouillas P. Thrombolysis for ischemic stroke in patients with old microbleeds on pretreatment MRI. Cerebrovasc. Dis. 2004; 17(2–3): 238–241.
79. Lee SH, Bae HJ, Kwon SJ, Kim H, Kim YH, Yoon BW, Roh JK. Cerebral microbleeds are regionally associated with intracerebral hemorrhage. Neurology 2004; 62(1): 72–76.
80. Theysohn JM, Kraff O, Maderwald S, Barth M, Ladd SC, Forsting M, Ladd ME, Gizewski ER. 7 tesla MRI of microbleeds and white matter lesions as seen in vascular dementia. J. Magn. Reson. Imaging 2011; 33(4): 782–791.
81. Mainero C, Benner T, Radding A, van der Kouwe A, Jensen R, Rosen BR, Kinkel RP. In vivo imaging of cortical pathology in multiple sclerosis using ultra-high field MRI. Neurology 2009; 73(12): 941–948.
82. Metcalf M, Xu D, Okuda DT, Carvajal L, Srinivasan R, Kelley DA, Mukherjee P, Nelson SJ, Vigneron DB, Pelletier D. High-resolution phased-array MRI of the human brain at 7 Tesla: initial experience in multiple sclerosis patients. J. Neuroimaging 2010; 20(2): 141–147.
83. Tallantyre EC, Morgan PS, Dixon JE, Al-Radaideh A, Brookes MJ, Morris PG, Evangelou N. 3 Tesla and 7 Tesla MRI of multiple sclerosis cortical lesions. J. Magn. Reson. Imaging 2010; 32(4): 971–977.
84. Tallantyre EC, Brookes MJ, Dixon JE, Morgan PS, Evangelou N, Morris PG. Demonstrating the perivascular distribution of MS lesions in vivo with 7-Tesla MRI. Neurology 2008; 70(22): 2076–2078.
85. Ge Y, Zohrabian VM, Grossman RI. Seven-tesla magnetic resonance imaging: new vision of microvascular abnormalities in multiple sclerosis. Arch. Neurol. 2008; 65(6): 812–816.
86. Tallantyre EC, Morgan PS, Dixon JE, Al-Radaideh A, Brookes MJ, Evangelou N, Morris PG. A comparison of 3 T and 7 T in the detection of small parenchymal veins within MS lesions. Invest. Radiol. 2009; 44(9): 491–494.
87. Hammond KE, Metcalf M, Carvajal L, Okuda DT, Srinivasan R, Vigneron D, Nelson SJ, Pelletier D. Quantitative in vivo magnetic resonance imaging of multiple sclerosis at 7 Tesla with sensitivity to iron. Ann. Neurol. 2008; 64(6): 707–713.
88. von Morze C, Xu D, Purcell DD, Hess CP, Mukherjee P, Saloner D, Kelley DA, Vigneron DB. Intracranial time-of-flight MR angiography at 7 T with comparison to 3 T. J. Magn. Reson. Imaging 2007; 26(4): 900–904.
89. Heverhagen JT, Bourekas E, Sammet S, Knopp MV, Schmalbrock P. Time-of-flight magnetic resonance angiography at 7 Tesla. Invest. Radiol. 2008; 43(8): 568–573.
90. Kang CK, Hong SM, Han JY, Kim KN, Kim SH, Kim YB, Cho ZH. Evaluation of MR angiography at 7.0 Tesla MRI using birdcage radio frequency coils with end caps. Magn. Reson. Med. 2008; 60(2): 330–338.
91. Cho ZH, Kang CK, Han JY, Kim SH, Kim KN, Hong SM, Park CW, Kim YB. Observation of the lenticulostriate arteries in the human brain in vivo using 7.0 T MR angiography. Stroke 2008; 39(5): 1604–1606.
92. Kang CK, Park CW, Han JY, Kim SH, Park CA, Kim KN, Hong SM, Kim YB, Lee KH, Cho ZH. Imaging and analysis of lenticulostriate arteries using 7.0-Tesla magnetic resonance angiography. Magn. Reson. Med. 2009; 61(1): 136–144.
93. Conijn MM, Hendrikse J, Zwanenburg JJ, Takahara T, Geerlings MI, Mali WP, Luijten PR. Perforating arteries originating from the posterior communicating artery: a 7.0-Tesla MRI study. Eur. Radiol. 2009; 19(12): 2986–2992.
94. Maderwald S, Ladd SC, Gizewski ER, Kraff O, Theysohn JM, Wicklow K, Moenninghoff C, Wanke I, Ladd ME, Quick HH. To TOF or not to TOF: strategies for non-contrast-enhanced intracranial MRA at 7 T. MAGMA 2008; 21(1–2): 159–167.
95. Zwanenburg JJ, Hendrikse J, Takahara T, Visser F, Luijten PR. MR angiography of the cerebral perforating arteries with magnetization prepared anatomical reference at 7 T: comparison with time-of-flight. J. Magn. Reson. Imaging 2008; 28(6): 1519–1526.
96. Van de Moortele PF, Auerbach EJ, Olman C, Yacoub E, Ugurbil K, Moeller S. T1 weighted brain images at 7 Tesla unbiased for proton density, T2* contrast and RF coil receive B1 sensitivity with simultaneous vessel visualization. Neuroimage 2009; 46(2): 432–446.
97. Marques JP, Kober T, Krueger G, van der Zwaag W, Van de Moortele PF, Gruetter R. MP2RAGE, a self bias-field corrected sequence for improved segmentation and T1-mapping at high field. Neuroimage 2010; 49(2): 1271–1281.
98. Monninghoff C, Maderwald S, Theysohn JM, Kraff O, Ladd SC, Ladd ME, Forsting M, Quick HH, Wanke I. Evaluation of intracranial aneurysms with 7 T versus 1.5 T time-of-flight MR angiography—initial experience. Rofo 2009; 181(1): 16–23.
99. Monninghoff C, Maderwald S, Wanke I. Pre-interventional assessment of a vertebrobasilar aneurysm with 7 tesla time-of-flight MR angiography. Rofo 2009; 181(3): 266–268.
100. Schlamann M, Maderwald S, Becker W, Kraff O, Theysohn JM, Mueller O, Sure U, Wanke I, Ladd ME, Forsting M, Schaefer L, Gizewski ER. Cerebral cavernous hemangiomas at 7 Tesla: initial experience. Acad. Radiol. 2010; 17(1): 3–6.
101. Dammann P, Barth M, Zhu Y, Maderwald S, Schlamann M, Ladd ME, Sure U. Susceptibility weighted magnetic resonance imaging of cerebral cavernous malformations: prospects, drawbacks, and first experience at ultra-high field strength (7-Tesla) magnetic resonance imaging. Neurosurg. Focus 2010; 29(3): E5.
102. Brandauer B, Hermsdorfer J, Beck A, Aurich V, Gizewski ER, Marquardt C, Timmann D. Impairments of prehension kinematics and grasping forces in patients with cerebellar degeneration and the relationship to cerebellar atrophy. Clin. Neurophysiol. 2008; 119(11): 2528–2537.
103. Schulz JB, Borkert J, Wolf S, Schmitz-Hubsch T, Rakowicz M, Mariotti C, Schoels L, Timmann D, van de Warrenburg B, Durr A, Pandolfo M,

Kang JS, Mandly AG, Nagele T, Grisoli M, Boguslawska R, Bauer P, Klockgether T, Hauser TK. Visualization, quantification and correlation of brain atrophy with clinical symptoms in spinocerebellar ataxia types 1, 3 and 6. Neuroimage 2010; 49(1): 158–168.
104. Kuper M, Thurling M, Maderwald S, Ladd ME, Timmann D. Structural and functional magnetic resonance imaging of the human cerebellar nuclei. Cerebellum 2010; DOI: 10.1007/s12311-010-0194-5 [Epub ahead of print].
105. Berg D, Youdim MB. Role of iron in neurodegenerative disorders. Top. Magn. Reson. Imaging 2006; 17(1): 5–17.
106. Chavhan GB, Babyn PS, Thomas B, Shroff MM, Haacke EM. Principles, techniques, and applications of T2*-based MR imaging and its special applications. Radiographics 2009; 29(5): 1433–1449.
107. Marques JP, Maddage R, Mlynarik V, Gruetter R. On the origin of the MR image phase contrast: an in vivo MR microscopy study of the rat brain at 14.1 T. Neuroimage 2009; 46(2): 345–352.
108. Koeppen AH. The pathogenesis of spinocerebellar ataxia. Cerebellum 2005; 4(1): 62–73.
109. Windischberger C, Fischmeister FP, Schopf V, Sladky R, Moser E. Functional magnetic resonance imaging with ultra-high fields. Radiologe 2010; 50(2): 144–151.
110. Poser BA, Norris DG. Investigating the benefits of multi-echo EPI for fMRI at 7 T. Neuroimage 2009; 45(4): 1162–1172.
111. Beisteiner R, Robinson S, Wurnig M, Hilbert M, Merksa K, Rath J, Hollinger I, Klinger N, Marosi C, Trattnig S, Geissler A. Clinical fMRI: evidence for a 7 T benefit over 3 T. Neuroimage 2011; 57(3): 1015–1021.
112. Timmann D, Daum I. Cerebellar contributions to cognitive functions: a progress report after two decades of research. Cerebellum 2007; 6(3): 159–162.
113. Strick PL, Dum RP, Fiez JA. Cerebellum and nonmotor function. Annu. Rev. Neurosci. 2009; 32: 413–434.
114. Dimitrova A, de Greiff A, Schoch B, Gerwig M, Frings M, Gizewski ER, Timmann D. Activation of cerebellar nuclei comparing finger, foot and tongue movements as revealed by fMRI. Brain Res. Bull. 2006; 71(1–3): 233–241.
115. Habas C. Functional imaging of the deep cerebellar nuclei: a review. Cerebellum 2010; 9(1): 22–28.
116. Di Ieva A, Tschabitscher M, Galzio RJ, Grabner G, Kronnerwetter C, Widhalm G, Matula C, Trattnig S. The veins of the nucleus dentatus: anatomical and radiological findings. Neuroimage 2011; 54(1): 74–79.
117. Logothetis NK, Wandell BA. Interpreting the BOLD signal. Annu. Rev. Physiol. 2004; 66: 735–769.
118. Logothetis N, Merkle H, Augath M, Trinath T, Ugurbil K. Ultra high-resolution fMRI in monkeys with implanted RF coils. Neuron 2002; 35(2): 227–242.
119. Küper M, Dimitrova A, Thürling M, Maderwald S, Roths J, Elles HG, Gizewski ER, Ladd ME, Diedrichsen J, Timmann D. Evidence for a motor and a non-motor domain in the human dentate nucleus—an fMRI study. Neuroimage 2011; 54(4): 2612–2622.
120. Habas C, Guillevin R, Abanou A. In vivo structural and functional imaging of the human rubral and inferior olivary nuclei: a mini-review. Cerebellum 2010; 9(2): 167–173. Review
121. Fillippi M (ed). Part II: FMRI Application to Measure Brain Function. In *FMRI Techniques and Protocols*, Walz W series editor (ed). Humana Press, Springer: 2009; 285–569.
122. Mlynarik V, Gruber S, Moser E. Proton T (1) and T (2) relaxation times of human brain metabolites at 3 Tesla. NMR Biomed. 2001; 14(5): 325–331.
123. Gonen O, Gruber S, Li BS, Mlynarik V, Moser E. Multivoxel 3D proton spectroscopy in the brain at 1.5 versus 3.0 T: signal-to-noise ratio and resolution comparison. Am. J. Neuroradiol. 2001; 22(9): 1727–1731.
124. Gruber S, Mlynarik V, Moser E. High-resolution 3D proton spectroscopic imaging of the human brain at 3 T: SNR issues and application for anatomy-matched voxel sizes. Magn. Reson. Med. 2003; 49(2): 299–306.
125. Bogner W, Gruber S, Doelken M, Stadlbauer A, Ganslandt O, Boettcher U, Trattnig S, Doerfler A, Stefan H, Hammen T. In vivo quantification of intracerebral GABA by single-voxel (1)H-MRS—how reproducible are the results? Eur. J. Radiol. 2010; 73(3): 526–531.
126. Mekle R, Mlynarik V, Gambarota G, Hergt M, Krueger G, Gruetter R. MR spectroscopy of the human brain with enhanced signal intensity at ultrashort echo times on a clinical platform at 3 T and 7 T. Magn. Reson. Med. 2009; 61(6): 1279–1285.
127. Tkac I, Oz G, Adriany G, Ugurbil K, Gruetter R. In vivo ^{1}H NMR spectroscopy of the human brain at high magnetic fields: metabolite quantification at 4 T vs. 7 T. Magn. Reson. Med. 2009; 62(4): 868–879.
128. Carlsson A, Ljungberg M, Starck G, Forssell-Aronsson E. Degraded water suppression in small volume (1)H MRS due to localised shimming. MAGMA 2011; 24(2): 97–107.
129. Ganslandt O, Stadlbauer A, Fahlbusch R, Kamada K, Buslei R, Blumcke I, Moser E, Nimsky C. Proton magnetic resonance spectroscopic imaging integrated into image-guided surgery: correlation to standard magnetic resonance imaging and tumor cell density. Neurosurgery 2005; 56(2 Suppl): 291–298; discussion 291–298.
130. Boer VO, Siero JC, Hoogduin H, van Gorp JS, Luijten PR, Klomp DW. High-field MRS of the human brain at short TE and TR. NMR Biomed. 2011; 24(9): 1081–1088.
131. Snyder J, Wilman A. Field strength dependence of PRESS timings for simultaneous detection of glutamate and glutamine from 1.5 to 7 T. J. Magn. Reson. 2010; 203(1): 66–72.
132. Pan JW, Avdievich N, Hetherington HP. J-refocused coherence transfer spectroscopic imaging at 7 T in human brain. Magn. Reson. Med. 2010; 64(5): 1237–1246.
133. Gambarota G, Mekle R, Xin L, Hergt M, van der Zwaag W, Krueger G, Gruetter R. In vivo measurement of glycine with short echo-time ^{1}H MRS in human brain at 7 T. MAGMA 2009; 22(1): 1–4.
134. Bogner W, Gruber S, Trattnig S, Chmelik M. High-resolution mapping of human brain metabolites by proton FID-MRSI at 7 T. NMR Biomed. 2011; in press.
135. Hetherington H. Novel approaches to imaging epilepsy by MRI. Future Neurol. 2009; 4(3): 295–304.
136. Bogner W, Chmelik M, Andronesi OC, Sorensen AG, Trattnig S, Gruber S. In vivo (31) P spectroscopy by fully adiabatic extended image selected in vivo spectroscopy: a comparison between 3 T and 7 T. Magn. Reson. Med. 2011; 66(4): 923–930.
137. Stephenson MC, Gunner F, Napolitano A, Greenhaff PL, Macdonald IA, Saeed N, Vennart W, Francis ST, Morris PG. Applications of multinuclear magnetic resonance spectroscopy at 7 T. World J. Radiol. 2011; 3(4): 105–113.
138. Krug R, Stehling C, Kelley DA, Majumdar S, Link TM. Imaging of the musculoskeletal system in vivo using ultra-high field magnetic resonance at 7 T. Invest. Radiol. 2009; 44(9): 613–618.
139. Regatte RR, Schweitzer ME. Ultra-high-field MRI of the musculoskeletal system at 7.0 T. J. Magn. Reson. Imaging 2007; 25(2): 262–269.
140. Friedrich KM, Chang G, Vieira RL, Wang L, Wiggins GC, Schweitzer ME, Regatte RR. In vivo 7.0-tesla magnetic resonance imaging of the wrist and hand: technical aspects and applications. Semin. Musculoskelet. Radiol. 2009; 13(1): 74–84.
141. Goldstein SA, Goulet R, McCubbrey D. Measurement and significance of three-dimensional architecture to the mechanical integrity of trabecular bone. Calcif. Tissue Int. 1993; 53(Suppl 1): S127–132; discussion S132–133.
142. Kleerekoper M, Villanueva AR, Stanciu J, Rao DS, Parfitt AM. The role of three-dimensional trabecular microstructure in the pathogenesis of vertebral compression fractures. Calcif. Tissue Int. 1985; 37(6): 594–597.
143. Borah B, Dufresne TE, Chmielewski PA, Gross GJ, Prenger MC, Phipps RJ. Risedronate preserves trabecular architecture and increases bone strength in vertebra of ovariectomized minipigs as measured by three-dimensional microcomputed tomography. J. Bone Miner. Res. 2002; 17(7): 1139–1147.
144. Ding M, Odgaard A, Linde F, Hvid I. Age-related variations in the microstructure of human tibial cancellous bone. J. Orthop. Res. 2002; 20(3): 615–621.
145. Krug R, Carballido-Gamio J, Banerjee S, Stahl R, Carvajal L, Xu D, Vigneron D, Kelley DA, Link TM, Majumdar S. In vivo bone and cartilage MRI using fully-balanced steady-state free-precession at 7 tesla. Magn. Reson. Med. 2007; 58(6): 1294–1298.
146. Hopkins JA, Wehrli FW. Magnetic susceptibility measurement of insoluble solids by NMR: magnetic susceptibility of bone. Magn. Reson. Med. 1997; 37(4): 494–500.
147. Chang G, Regatte RR, Schweitzer ME. Olympic fencers: adaptations in cortical and trabecular bone determined by quantitative computed tomography. Osteoporos. Int. 2009; 20(5): 779–785.
148. Stahl R, Krug R, Kelley DA, Zuo J, Ma CB, Majumdar S, Link TM. Assessment of cartilage-dedicated sequences at ultra-high-field MRI: comparison of imaging performance and diagnostic confidence

between 3.0 and 7.0 T with respect to osteoarthritis-induced changes at the knee joint. Skeletal Radiol. 2009; 38(8): 771–783.
149. Kraff O, Theysohn JM, Maderwald S, Saylor C, Ladd SC, Ladd ME, Barkhausen J. MRI of the knee at 7.0 Tesla. Rofo 2007; 179(12): 1231–1235.
150. Mosher TJ, Dardzinski BJ. Cartilage MRI T2 relaxation time mapping: overview and applications. Semin. Musculoskelet. Radiol. 2004; 8(4): 355–368.
151. Smith HE, Mosher TJ, Dardzinski BJ, Collins BG, Collins CM, Yang QX, Schmithorst VJ, Smith MB. Spatial variation in cartilage T2 of the knee. J. Magn. Reson. Imaging 2001; 14(1): 50–55.
152. Welsch GH, Mamisch TC, Hughes T, Zilkens C, Quirbach S, Scheffler K, Kraff O, Schweitzer ME, Szomolanyi P, Trattnig S. In vivo biochemical 7.0 Tesla magnetic resonance: preliminary results of dGEMRIC, zonal T2, and T2* mapping of articular cartilage. Invest. Radiol. 2008; 43(9): 619–626.
153. Pakin SK, Cavalcanti C, La Rocca R, Schweitzer ME, Regatte RR. Ultra-high-field MRI of knee joint at 7.0 T: preliminary experience. Acad. Radiol. 2006; 13(9): 1135–1142.
154. Murphy BJ. Evaluation of grades 3 and 4 chondromalacia of the knee using T2*-weighted 3D gradient-echo articular cartilage imaging. Skeletal Radiol. 2001; 30(6): 305–311.
155. Hughes T, Welsch GH, Trattnig S, Brandi L, Domayer S, Mamisch TC. T2-star relaxation as a means to differentiatie cartilage repair tissue after microfracturing therapy. Int. Soc. Magn. Reson. Med. 2007; 15: 183.
156. Wietek B, Martirosian P, Machann J, Mueller-Horvath C, Claussen CD, Schick F. T2 and T2* mapping of the human femoral-tibial cartilage at 1.5 and 3 Tesla. Int. Soc. Magn. Reson. Med. 2007; 15: 516.
157. Mankin HJ. Biochemical and metabolic aspects of osteoarthritis. Orthoped. Clin. N. Am. 1971; 2(1): 19–31.
158. Roughley PJ, Lee ER. Cartilage proteoglycans: structure and potential functions. Microsc. Res. Tech. 1994; 28(5): 385–397.
159. Lohmander LS. Articular cartilage and osteoarthrosis. The role of molecular markers to monitor breakdown, repair and disease. J. Anat. 1994; 184(Pt 3): 477–492.
160. Grushko G, Schneiderman R, Maroudas A. Some biochemical and biophysical parameters for the study of the pathogenesis of osteoarthritis: a comparison between the processes of ageing and degeneration in human hip cartilage. Connect. Tissue Res. 1989; 19(2–4): 149–176.
161. Maroudas A, Muir H, Wingham J. The correlation of fixed negative charge with glycosaminoglycan content of human articular cartilage. Biochim. Biophys. Acta 1969; 177(3): 492–500.
162. Borthakur A, Shapiro EM, Beers J, Kudchodkar S, Kneeland JB, Reddy R. Sensitivity of MRI to proteoglycan depletion in cartilage: comparison of sodium and proton MRI. Osteoarthr. Cartil. 2000; 8(4): 288–293.
163. Shapiro EM, Borthakur A, Gougoutas A, Reddy R. ^{23}Na MRI accurately measures fixed charge density in articular cartilage. Magn. Reson. Med. 2002; 47(2): 284–291.
164. Borthakur A, Shapiro EM, Akella SV, Gougoutas A, Kneeland JB, Reddy R. Quantifying sodium in the human wrist in vivo by using MR imaging. Radiology 2002; 224(2): 598–602.
165. Burstein D, Velyvis J, Scott KT, Stock KW, Kim YJ, Jaramillo D, Boutin RD, Gray ML. Protocol issues for delayed Gd(DTPA)(2–)-enhanced MRI (dGEMRIC) for clinical evaluation of articular cartilage. Magn. Reson. Med. 2001; 45(1): 36–41.
166. Hoult DI, Chen CN, Sank VJ. The field dependence of NMR imaging. II. Arguments concerning an optimal field strength. Magn. Reson. Med. 1986; 3(5): 730–746.
167. Chen CN, Sank VJ, Cohen SM, Hoult DI. The field dependence of NMR imaging. I. Laboratory assessment of signal-to-noise ratio and power deposition. Magn. Reson. Med. 1986; 3(5): 722–729.
168. Snyder CJ, DelaBarre L, Metzger GJ, van de Moortele PF, Akgun C, Ugurbil K, Vaughan JT. Initial results of cardiac imaging at 7 Tesla. Magn. Reson. Med. 2009; 61(3): 517–524.
169. van den Bergen B, Van den Berg CA, Bartels LW, Lagendijk JJ. 7 T body MRI: B1 shimming with simultaneous SAR reduction. Phys. Med. Biol. 2007; 52(17): 5429–5441.
170. Orzada S, Maderwald S, Poser BA, Bitz AK, Quick HH, Ladd ME. RF excitation using time interleaved acquisition of modes (TIAMO) to address B1 inhomogeneity in high-field MRI. Magn. Reson. Med. 2010; 64(2): 327–333.
171. Orzada S, Quick H, Ladd M, Bahr A, Bolz T, Yazdanbakhsh P, Solbach K, Bitz A. A flexible 8-channel transmit/receive body coil for 7 T human imaging. *Proceedings of the 17th Annual Meeting ISMRM*, Honolulu, HI, USA, 2009; 2999.
172. Orzada S, Maderwald S, Kraff O, Brote I, Ladd ME, Solbach K, Yazdanbakhsh P, Bahr A, Fautz HP, Bitz A. 16-channel Tx/Rx body coil for RF shimming with selected Cp modes at 7 T. *Proceedings of the 18th Annual Meeting ISMRM*, Stockholm, Sweden, 2010; 50.
173. Umutlu L, Bitz AK, Maderwald S, Orzada S, Kinner S, Kraff O, Brote I, Ladd SC, Antoch G, Ladd ME, Quick HH, Lauenstein TC. 7 T liver MRI in humans: initial results. *Proceedings of the 18th Annual Meeting ISMRM*, Stockholm, Sweden, 2010; 2624.
174. Umutlu L, Kraff O, Orzada S, Fischer A, Kinner S, Maderwald S, Antoch G, Quick HH, Forsting M, Ladd ME, Lauenstein TC. Dynamic contrast-enhanced renal MRI at 7 Tesla: preliminary results. Invest. Radiol. 2011; 46(7): 425–433.
175. Umutlu L, Orzada S, Kinner S, Maderwald S, Brote I, Bitz AK, Kraff O, Ladd SC, Antoch G, Ladd ME, Quick HH, Lauenstein TC. Renal imaging at 7 Tesla: preliminary results. Eur. Radiol. 2011; 21(4): 841–849.
176. Darwish T, Wood B. Nephrogenic systemic fibrosis: what internists need to know. Mo. Med. 2009; 106(5): 373–376.
177. Grinstead JW, Rooney W, Laub G. The origins of bright blood MPRAGE at 7 Tesla and a simultaneous method for T1 imaging and non-contrast MRA. *Proceedings of the 18th Annual Meeting ISMRM*, Stockholm, Sweden, 2010; 1429.
178. Niendorf T, Sodickson DK, Krombach GA, Schulz-Menger J. Toward cardiovascular MRI at 7 T: clinical needs, technical solutions and research promises. Eur. Radiol. 2010; 20(12): 2806–2816.
179. Brandts A, Westenberg JJ, Versluis MJ, Kroft LJ, Smith NB, Webb AG, de Roos A. Quantitative assessment of left ventricular function in humans at 7 T. Magn. Reson. Med. 2010; 64(5): 1471–1477.
180. von Knobelsdorff-Brenkenhoff F, Frauenrath T, Prothmann M, Dieringer MA, Hezel F, Renz W, Kretschel K, Niendorf T, Schulz-Menger J. Cardiac chamber quantification using magnetic resonance imaging at 7 Tesla—a pilot study. Eur. Radiol. 2010; 20(12): 2844–2852.
181. van Elderen SG, Versluis MJ, Webb AG, Westenberg JJ, Doornbos J, Smith NB, de Roos A, Stuber M. Initial results on in vivo human coronary MR angiography at 7 T. Magn. Reson. Med. 2009; 62(6): 1379–1384.
182. van Elderen SG, Versluis MJ, Westenberg JJ, Agarwal H, Smith NB, Stuber M, de Roos A, Webb AG. Right coronary MR angiography at 7 T: a direct quantitative and qualitative comparison with 3 T in young healthy volunteers. Radiology 2010; 257(1): 254–259.
183. Abi-Abdallah D, Robin V, Drochon A, Fokapu O. Alterations in human ECG due to the MagnetoHydroDynamic effect: a method for accurate R peak detection in the presence of high MHD artifacts. Conf. Proc. IEEE Eng. Med. Biol. Soc. 2007; 2007: 1842–1845.
184. Frauenrath T, Hezel F, Heinrichs U, Kozerke S, Utting JF, Kob M, Butenweg C, Boesiger P, Niendorf T. Feasibility of cardiac gating free of interference with electro-magnetic fields at 1.5 Tesla, 3.0 Tesla and 7.0 Tesla using an MR-stethoscope. Invest. Radiol. 2009; 44(9): 539–547.
185. Frauenrath T, Hezel F, Renz W, d'Orth Tde G, Dieringer M, von Knobelsdorff-Brenkenhoff F, Prothmann M, Menger JS, Niendorf T. Acoustic cardiac triggering: a practical solution for synchronization and gating of cardiovascular magnetic resonance at 7 Tesla. J. Cardiovasc. Magn. Reson. 2010; 12: 67.
186. Wu B, Wang C, Krug R, Kelley DA, Xu D, Pang Y, Banerjee S, Vigneron DB, Nelson SJ, Majumdar S, Zhang X. 7 T human spine imaging arrays with adjustable inductive decoupling. IEEE Trans. Biomed. Eng. 2010; 57(2): 397–403.
187. Kraff O, Bitz AK, Kruszona S, Orzada S, Schaefer LC, Theysohn JM, Maderwald S, Ladd ME, Quick HH. An eight-channel phased array RF coil for spine MR imaging at 7 T. Invest. Radiol. 2009; 44(11): 734–740.
188. Vossen M, Teeuwisse W, Reijnierse M, Collins CM, Smith NB, Webb AG. A radiofrequency coil configuration for imaging the human vertebral column at 7 T. J. Magn. Reson. 2011; 208(2): 291–297.
189. Metzger GJ, Snyder C, Akgun C, Vaughan T, Ugurbil K, Van de Moortele PF. Local B1+ shimming for prostate imaging with transceiver arrays at 7 T based on subject-dependent transmit phase measurements. Magn. Reson. Med. 2008; 59(2): 396–409.
190. Klomp DW, Bitz AK, Heerschap A, Scheenen TW. Proton spectroscopic imaging of the human prostate at 7 T. NMR Biomed. 2009; 22(5): 495–501.

191. Klomp DW, Scheenen TW, Arteaga CS, van Asten J, Boer VO, Luijten PR. Detection of fully refocused polyamine spins in prostate cancer at 7 T. NMR Biomed. 2011; 24(3): 299–306.
192. Metzger GJ, van de Moortele PF, Akgun C, Snyder CJ, Moeller S, Strupp J, Andersen P, Shrivastava D, Vaughan T, Ugurbil K, Adriany G. Performance of external and internal coil configurations for prostate investigations at 7 T. Magn. Reson. Med. 2010; 64(6): 1625–1639.
193. van den Bergen B, Klomp DW, Raaijmakers AJ, de Castro CA, Boer VO, Kroeze H, Luijten PR, Lagendijk JJ, van den Berg CA. Uniform prostate imaging and spectroscopy at 7 T: comparison between a microstrip array and an endorectal coil. NMR Biomed. 2011; 24(4): 358–365.
194. Hecht EM, Lee RF, Taouli B, Sodickson DK. Perspectives on body MR imaging at ultrahigh field. Magn. Reson. Imaging Clin. N. Am. 2007; 15(3): 449–465, viii.
195. Umutlu L, Maderwald S, Kraff O, Theysohn JM, Kuemmel S, Hauth EA, Forsting M, Antoch G, Ladd ME, Quick HH, Lauenstein TC. Dynamic contrast-enhanced breast MRI at 7 Tesla utilizing a single-loop coil: a feasibility trial. Acad. Radiol. 2010; 17(8): 1050–1056.
196. Korteweg MA, Veldhuis WB, Visser F, Luijten PR, Mali WP, van Diest PJ, van den Bosch MA, Klomp DJ. Feasibility of 7 Tesla breast magnetic resonance imaging determination of intrinsic sensitivity and high-resolution magnetic resonance imaging, diffusion-weighted imaging, and ^{1}H-magnetic resonance spectroscopy of breast cancer patients receiving neoadjuvant therapy. Invest. Radiol. 2011; 46(6): 370–376.
197. Klomp DW, van de Bank BL, Raaijmakers A, Korteweg MA, Possanzini C, Boer VO, van de Berg CA, van de Bosch MA, Luijten PR. (31) P MRSI and (1) H MRS at 7 T: initial results in human breast cancer. NMR Biomed. 2011; DOI: 10.1002/nbm.1696. [Epub ahead of print].